UNIVERSITY OF TURKU

SURFACE AND BULK ANALYSIS OF Sr_2FeMoO_6 THIN FILMS – Sr_2FeMoO_6 BASED SPIN VALVE PROTOTYPE

Ilari Angervo

TURUN YLIOPISTON JULKAISUJA – ANNALES UNIVERSITATIS TURKUENSIS
SARJA – SER. AI OSA – TOM. 629 | ASTRONOMICA – CHEMICA – PHYSICA – MATHEMATICA | TURKU 2020

UNIVERSITY OF TURKU

SURFACE AND BULK ANALYSIS OF Sr_2FeMoO_6 THIN FILMS – Sr_2FeMoO_6 BASED SPIN VALVE PROTOTYPE

Ilari Angervo

TURUN YLIOPISTON JULKAISUJA – ANNALES UNIVERSITATIS TURKUENSIS
SARJA – SER. AI OSA – TOM. 629 | ASTRONOMICA – CHEMICA – PHYSICA – MATHEMATICA | TURKU 2020

University of Turku

Faculty of Science and Engineering
Department of Physics and Astronomy
Wihuri Physical Laboratory
Doctoral Programme in Physical and Chemical Sciences

Supervised by

Prof. Petriina Paturi
Wihuri Physical Laboratory
Dept. of Physics and Astronomy
University of Turku
Turku, Finland

Dr. Hannu Huhtinen
Wihuri Physical Laboratory
Dept. of Physics and Astronomy
University of Turku
Turku, Finland

Dr. Minnamari Saloaro
Wihuri Physical Laboratory
Dept. of Physics and Astronomy
University of Turku
Turku, Finland

Reviewed by

Prof. Maarit Karppinen
Department of Chemistry and
Materials Science
Aalto University
Espoo, Finland

Prof. Mikalai Kalanda
Scientific-Practical Materials Research
Centre of the National Academy of
Sciences of Belarus
19, P.Brovka Str.
220072 Minsk, Belarus

Opponent

Dr. Johan Lindén
Department of Physics
Åbo Akademi University
Turku, Finland

ISBN 978-951-29-8138-0 (PRINT)
ISBN 978-951-29-8139-7 (PDF)
ISSN 0082-7002 (Print)
ISSN 2343-3175 (Online)
Painosalama Oy, Turku, Finland 2020

Preface

Acknowledgments

This work has been carried out in the Wihuri Physical Laboratory of the Department of Physics and Astronomy at the University of Turku. The Jenny and Antti Wihuri Foundation, the University of Turku Graduate School and the University of Turku Foundation are acknowledged for their invaluable financial support. I wish to express my gratitude to Prof. Maarit Karppinen and Prof. Mikalai Kalanda for their insightful comments and reviewing of this thesis. I am specially grateful to Dr. Johan Lindén. It is an honor to have you as my opponent.

I wish to express my sincere gratitude to Prof. Petriina Paturi, for all the support and help that has been provided for organizing the scholarship applications, discussion on the thesis and the preceding work and also for creating an insightful and kind work place. For almost all the guidance and introduction to the laboratory work, I have to thank Dr. Minnamari Saloaro. Without her trustful guidance, this work could not have been finished as it is today. Of course for all the help in the laboratory work, discussion about the work and for the early introduction to warm-hearted people at the Wihuri laboratory, I wish to also thank Dr. Hannu Huhtinen. Many thanks also to Tapio Mäkelä and Sayani Majumdar for their contributions in the spin valve project included in this work.

Of course, this work would not have been possible without the loving support from family and friends. Specially I wish to thank Riikka Heikkilä for her loving support and kindness over the years.

Abstract

This thesis deals with the analysis of Sr_2FeMoO_6 (hereafter refered to as SFMO) thin films. The material is a part of a versatile double perovskite structure family and exhibits potential attributes for basic scientific interest and for spintronic application research. The introduction begins by outlining some of the features of SFMO as a material. The basic physics relevant for this work is also discussed.

The experimental work has been mostly carried out in the Wihuri Physical Laboratory and is largely build around the fabrication and the characterization of SFMO thin films. All the SFMO thin film samples have been deposited using a pulsed laser deposition equipment. The characterization includes a surface sensitive atomic and magnetic force microscopy along with a scanning tunneling microscopy technique. The surface sensitive spectroscopy analysis for electronic structure is done using x-ray photoelectron spectroscopy. In addition, the structural characterization includes a bulk sensitive x-ray diffraction technique and magnetometry measurements.

Based on the conducted work for the structural, magnetic and electronic characterization on the SFMO films, the effects of the deposition parameters are reported. The results demonstrate the influence of substrate materials, setting a possible threshold thickness for the films to overcome the interface defects and altering the orientation of the magnetization easy axis. The atomic force microscopy method showed an improvement in thin film surface structure, as lower surface roughness, with 900 °C deposition temperature compared with higher deposition temperatures. The surface structure of the SFMO films showed evidences of a single unit cell layer growth combined with island like growth. The electronic characterization revealed that the surface contamination in the SFMO films can be cleansed with *ex-situ* post-annealing. The annealing leads to significant valence fluctuation without any obvious unwanted side effects on SFMO.

As a finishing touch to this work, the recent advancement in spin valve deposition is reported. The results demonstrate, to our knowledge, the first spin valve effect in SFMO thin film based devices with an organic semiconductor transport layer. The results show a notable spin valve effect at low temperature. Magnetoresistance shows a clear decay with increasing temperature, but the magnetoresistance response close to room temperature is still observed.

Tiivistelmä

Tämä työ käsittelee Sr_2FeMoO_6 (SFMO) ohutkalvojen analyysiä. Materiaali on osa laajaa tuplaperovskiitti-rakenneryhmää. SFMO:lla on havaittu olevan perustutkimuksen kannalta mielenkiintoisia ominaisuuksia, mutta materiaali on myös kiinnostava spintroniikan sovellusten kannalta. Työ alkaa SFMO-materiaalin esittelyllä ja pohjustamalla työn kannalta oleellisia fysiikan osa-alueita.

Tämän työn kokeellinen tutkimus on pääosin tehty Wihurin fysiikantutkimuslaboratoriossa ja suuri osa työstä on SFMO-ohutkalvojen valmistusta ja ohutkalvojen karakterisointia. SFMO-ohutkalvot valmistettiin laserhöyrystysmenetelmällä. Tutkimus sisälsi pintaherkät atomi- ja magneettivoima- sekä tunnelointimikroskopiamittaukset. Röntgenfotoelektroniaspektroskopialla tutkittiin pintarakenteen elektronisia ominaisuuksia. Näytteitä tutkittiin myös röntgendiffraktiolla ja magnetometrimittauksilla.

Työn tuloksena raportoidaan kasvatusparametrien vaikutuksista SFMO-ohutkalvojen ominaisuuksiin. Esimerkkinä tulokset osoittavat alustamateriaalin vaikuttavan ohutkalvoihin asettaen raja-arvon ohutkalvojen paksuudelle, jolla alustamateriaalin aikaansaamien virheiden vaikutukset ovat lieviä. Alustamateriaali vaikuttaa myös kriittisesti ohutkalvojen magneettisen anisotropiaan. Atomivoimamikroskoopimittausten perusteella pintakarkeus on pienempi näytteillä, jotka on valmistettu verrattain alhaisessa 900 °C lämpötilassa. Pintarakenteessa havaitaan tunnelointimikroskopiamittausten avulla, että pinta kasvaa kaksiuloitteisesti yksikkökoppi kerrallaan. Kasvulla on kuitenkin useita kasvukeskuksia, mikä johtaa saarekkeiseen ohutkalvon kasvuun. Tutkimukset paljastavat, että pintakontaminaatiota voidaan poistaa *ex-situ* lämpökäsittelyllä. Käsittely aiheuttaa merkittävän valenssivaihtelun SFMO-ohutkalvoissa.Käsittelyllä ei havaita olevan negatiivista vaikutusta näytteiden ominaisuuksiin.

Työssä raportoidaan ennen julkaisemattomia tuloksia SFMO-ohutkalvoihin perustuvista spinventtiileistä. Käsittääksemme tulokset edustavat ensimmäisiä toimivia SFMO-ohutkalvoihin perustuvia spinventtiilejä, joissa virrankuljetuskerroksena ferromagneettisten kerrosten välissä on orgaaninen puolijohde. Tulokset osoittavat selkeän spinventtiilivasteen matalissa lämpötiloissa. Magnetoresistanssin nähdään heikkenevän selkeästi korkeammissa lämpötiloissa, mutta huomattava magnetoresistanssi havaitaan lähellä huonelämpötilaa.

Articles included in this thesis

This thesis is based on the experimental work carried out at the Wihuri Physical Laboratory, Department of Physics and Astronomy, University of Turku during the years 2015 – 2020. The thesis consists of an introductory part and of the following publications:

[**P1**] I. Angervo, M. Saloaro, H. Palonen, S. Majumdar, H. Huhtinen and P. Paturi: *Thickness dependent properties of Sr_2FeMoO_6 thin films grown on $SrTiO_3$ and $(LaAlO_3)_{0.3}(Sr_2AlTaO_6)_{0.7}$ substrates*, Physics Procedia **75**, 1011, (2015)

[**P2**] I. Angervo, M. Saloaro, J. Tikkanen, H. Huhtinen, P. Paturi: *Improving the surface structure of high quality Sr_2FeMoO_6 thin films for multilayer structures*, Appl. Surf. Sci. **396**, 754, (2017)

[**P3**] I. Angervo, M. Saloaro, H. Huhtinen, P. Paturi: *Interface defects induced vertical magnetic anisotropy in Sr_2FeMoO_6 thin films*, Appl. Surf. Sci. **422**, 682, (2017)

[**P4**] I. Angervo, M. Saloaro, J. Mäkelä, J. -P. Lehtiö, H. Huhtinen, P. Paturi: *Surface topography and electrical properties in Sr_2FeMoO_6 films studied at cryogenic temperatures*, J. Phys.: Conf. Ser. **969**, 012107 (2018)

[**P5**] I. Angervo, R. Siekkinen, M. Saloaro, H. Huhtinen, P. Paturi: *Sr_2FeMoO_6 thin films: effect of gas flow during deposition*, J. Magn. Magn. Mater. **475**, 121, (2018)

[**P6**] I. Angervo, M. Saloaro, S. Granroth, H. Huhtinen, P. Paturi: *Refined Sr_2FeMoO_6 interface realized with photoemission and magnetization analysis*, Appl. Surf. Sci. **507**, 144435, (2020)

[**P7**] I. Angervo, T. Mäkelä, S. Majumdar, M. Saloaro, H. Palonen, H. Huhtinen, P. Paturi: *Giant magnetoresistance response in Sr_2FeMoO_6 based organic spin valves*, Manuscript

Contents

1 Motivation

The interest towards to complex oxide Sr_2FeMoO_6, simplified as SFMO, in the near history has risen, at least in part, due to its promising attributes regarding possible spintronic applications. The notable features include 100% spin polarization combined with high Curie temperature around 420 K [1]. In spintronics the electron spin state, instead of only electron charge, is harnessed as an additional degree of freedom for technological use. This allegedly provides a base for less volatile, less energy consuming and faster information processing or storing. Spintronics requires a method of transport, detection and a source of spin information. This is where SFMO becomes potential. Due to 100% spin polarization of the charge carriers and high Curie temperature, the material has become particular interest as a material for spintronics.

Perhaps the best known example of spintronic applications is a multilayered system consisting of two spin polarized ferromagnetic layers separated by a spin transport layer, where the resistivity of the system is controlled by the relative orientation of the magnetic moments in the magnetizations between the two ferromagnetic layers. This type of structure with such function is called a spin valve, or a pseudo-spin valve. Higher spin polarization would ideally result in a more profound response in resistivity with the alteration of the magnetic moments.

This thesis deals with the thin film analysis of SFMO. The work includes the bulk analysis of the magnetic and the structural thin film properties. This contributes to the improvement and to the understanding the effect of the deposition conditions and to the understanding of the intrinsic properties of the double perovskite SFMO. However, emphasis is given to surface analysis. In part this is done in order to provide a more accurate picture about SFMO thin film surface, which would act as the initial interface, between the transport layer and the ferromagnetic (ferrimagnetic) layer in the spin valve structure. The motivation for this arises due to the fact, while intrinsic properties of SFMO are undoubtedly important, the highly promising attributes can become irrelevant if the interface of the layered structure is flawed. This could mean pinholes from one ferromagnetic material to another through surface roughness, which could severely diminish the magnetoresistive response amplitude due to local ferromagnetic coupling [2]. One way to medicate the risk of pinholes is to increase the separation between the two ferromagnets. This however ultimately results in the loss of spin polarization in the current transport through the separating layer. Another problem, arising from the surface roughness, is the Néel coupling between ferromagnetic layers [3], which can affect the switching of the magnetic layers and hence the perfomance of the device. The

surface also provides the symmetry break from the bulk and is also a considerable area for the basic research and characterization. As an example the electronic structure of SFMO thin film surface is analyzed in this work. As an important achievement in this work, the results for recent advancement in spin valve fabrication are reported. The approach to the spin valve fabrication is taken by utilizing an organic semiconductor for the spin transport, allowing flexibility to the device structure. To our knowledge, this is the first time when SFMO has been adopted successfully in organic spin valves.

2 Introduction

2.1 Sr_2FeMoO_6

2.1.1 Perovskite structure of Sr_2FeMoO_6

Perovskites are a group of compounds that are close to or are derived from a general composition formula of ABX_3 [4, p. 1]. In the formula, A and B are usually a large- and a medium-sized cation, respectively. X counts for an anion [4, p. 1]. A schematic illustration of $SrTiO_3$ (STO) perovskite structure unit cell is presented in Figure 1 as an example of ABX_3 perovskite. When more ionic elements are present in a proper ratio, more complex perovskite structures can arise, like double or triple perovskite structures [4, p. 42]. The ideal Sr_2FeMoO_6 has a double perovskite structure and falls under the category described by a general formula of $A_2BB^{'}O_6$. The crystal structure of a double perovskite can be thought of as a system of ordered alternate octahedra containing a cation in different oxidation states [5, p. 502]. A composition with the general formula of $A_2BB^{'}O_6$, inside an octahedron there is either B or $B^{'}$ site cation, which in the case of SFMO is either heterovalent transition metal Fe or Mo. The alteration of B and $B^{'}$ cations in the crystal structure produces a rock-salt type ordering, meaning that each octahedron containing Fe cation is linked through an oxygen bond to another octahedron containing Mo cation and vice versa. Alkaline earth metal Sr is located in the center of the cube formed by the four closest oxygen octahedra. Sometimes, due to the comparison of unit cell sizes between SFMO and other perovskites, it is useful to view SFMO lattice in tetragonal symmetry. The tetragonal unit cell with the elemental sites is presented in Figure 1. The reference literature values used in this work for tetragonal SFMO lattice are based on the results reported by Nakamura *et.al*. [6]. These results provide a tetragonal lattice with lattice parameters $a = b = 5.575$ Å and $c = 7.893$ Å and space group I 4/m.

A real crystal structure of a solid is always accompanied by structural defects. One of the structural defects in solids is an antisite defect. An antisite defect is a structural defect where a site, ideally occupied by one element, is occupied by another element from the compound [7]. In SFMO, antisite disorder (ASD) in general refers to the misplacement between Fe and Mo cations. The concentration of antisite defects in SFMO can be, and has been, analyzed by x-ray diffraction since Fe/Mo disorder influences the relative diffraction peak intensities [8–10]. The element site in the unit cell can also remain empty, thereby creating a vacancy in the crystal structure. In principle the vacancy can appear at any site. However, the role of oxygen vacancies in SFMO has been

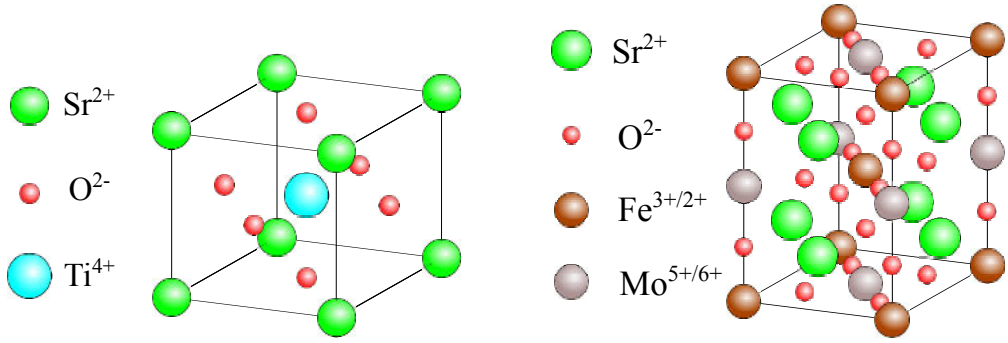

Figure 1. Illustration of the perovskite crystal structure unit cell for $SrTiO_3$ (left). Illustration of the double perovskite unit cell of tetragonal lattice for Sr_2FeMoO_6 (right).

the particular interest of research [11–14]. The role of oxygen vacancies and ASD on the magnetic properties are described in more detail in the following chapter. Besides antisite defects and vacancies in SFMO crystal, the phase purity can be diminished by secondary phases. Impurities are common defects in polycrystalline SFMO bulk and in SFMO films and arise especially due to unoptimized fabrication [15–19]**[P2]**. Confirmed impurity phases in SFMO include for example $SrMoO_4$, $SrMoO_3$ Fe_2O_3, Fe_3O_4 and $SrFeO_3$ [15–19]**[P2]**.

Due to external stress, the lattice parameters can be shortened or elongated. Other structural deformations are also possible. The deviation from the relaxed lattice parameters is described by lattice strain. The lattice strain in thin films can be defined according to the formula $\varepsilon = (l_{\text{film}} - l_{\text{bulk}})/l_{\text{bulk}}$, where l_{film} refers to the lattice parameter of the film and l_{bulk} refers to the bulk, or unstrained lattice parameter. The effects of the lattice strain show possible stabilization of SFMO lattice from the ASD, under the compressive strain [20]. The strain can also lower the formation energy of oxygen vacancies and the formation energies of other lattice defects are also affected [20].

2.1.2 Magnetic features in Sr_2FeMoO_6

Many perovskite compounds exhibit versatile intrinsic properties. These include, but are not limited to, colossal magnetoresistance, high temperature superconductivity and ferroelectricity [21]. One of the most highly considered attributes in the double perovskite SFMO is that the material exhibits a large low field magnetoresistance response below the ferro−paramagnetic transition temperature [1]. In a polycrystalline form, the low field magnetoresistance is linked to spin polarized tunneling of charge carriers

between individual grains. The charge carriers in the ideal SFMO structure are, according to the band structure calculations, 100% spin polarized [1]. This makes SFMO a half-metallic material. Half-metallicity arises from the fact that in the ideal SFMO, density of states has no available states in one of the two spin polarized bands at the Fermi level. In SFMO this band gap at the Fermi level lies in the spin-up band [1]. The magnetoresistance due to tunneling of spin polarized charge carriers is only seen below Curie temperature (T_C). In SFMO T_C is above room temperature, around 420 K [1].

The quantum mechanical exchange interaction between elements in the ideal SFMO crystal results in an antiferromagnetic ordering between Fe and Mo states [22]. The exchange interaction is mediated by an oxygen anion. The nature of the exchange interaction is usually described through double exchange type interaction [23, 24] although apparently an accurate description of the exchange interaction in SFMO seems to remain somewhat elusive. Due to unequal magnetic moments associated with Fe and Mo, the antiferromagnetic ordering becomes ferrimagnetic. SFMO is reported to exhibit a mixed valence both in Mo and in Fe, producing a degenerate ferrimagnetic ordering between Fe^{2+}/Mo^{6+} and Fe^{3+}/Mo^{5+} states [24, 25]. Both configurations result in the same theoretical saturation magnetization (M_{sat}) of 4 μ_B/f.u., when Fe^{2+} and Mo^{6+} (or Fe^{3+} and Mo^{5+}) are coupled antiferromagnetically. The saturation magnetization of 4 μ_B/f.u. equals the saturation magnetic moment in one SFMO unit formula.

Once SFMO crystal is altered from the ideal and structural defects are introduced, profound changes on the magnetic and the magnetoresistive properties can appear. The ASD, where a portion of the Fe and Mo sites have switched positions in the lattice structure, and its effects on the magnetic and the magnetoresistive properties have been studied exhaustively [9, 14, 26, 27, 29–33]. It is established that the ASD leads to an antiferromagnetic alignment between the two nearest Fe states [27, 33]. When the ferromagnetic alignment between the two nearest Fe states is changed to antiferromagnetic by the ASD, M_{sat} is diminished. However, it has been suggested that instead of an antiferromagnetic coupling between the nearest Fe sites in the mis-site defect, the decrease in the M_{sat} happens through the decrease of the net magnetic moment in individual Fe sites, while maintaining the ferromagnetic alignment [26], meaning that in a mis-site, the nearest Fe sites couple ferromagnetically. Although this argument would seem to be a less popular explanation for the decrease of the M_{sat}. The nearest Mo states in the ASD are paramagnetic and do not contribute for the saturation [27, 28]. It is also reported that the ASD, in high enough concentrations, destroys the spin polarization of charge carriers [26, 34]. This again has a direct effect on the magnetoresistance. Once the spin

polarization is decreased enough, the low field magnetoresistance is lost [9]. Based on both theoretical calculations and experiments, the T_C of SFMO is also decreased by the ASD [13, 27, 35]. Although according to theoretical investigation, with high enough ASD concentration due to a strong antiferromagnetic coupling between Fe−O−Fe, T_C is increased [13].

The role of oxygen vacancies in the magnetic features of SFMO has also been studied [11, 13, 14, 31, 32, 36–38]. Based on the current understanding, oxygen vacancies would increase the T_C and decrease the M_{sat} [13, 14]. The increase in the T_C via oxygen vacancies has been explained with the influence on the magnetic exchange interaction. While in defect free SFMO, there is a strong antiferromagnetic coupling between the nearest Fe and Mo states with the ferromagnetic coupling between the nearest Fe states, a weaker antiferromagnetic coupling character exists between the next nearest Fe states. Randomly distributed oxygen vacancies favor and strengthen the antiferromagnetic coupling, between Fe and Mo states, and weaken the antiferromagnetic coupling, between the next nearest Fe states, resulting in an increase in the T_C [14]. The half-metallicity can also be preserved when oxygen vacancies are present [14, 36, 38]. The effects of strain on the magnetic properties are partially due to the effects on the other defect types. Based on the theoretical band structure calculation, a simple alteration of lattice parameter sizes shows, that the half metallicity might be lost in strained films with sufficiently large strain [39]. In other investigations, the band gap has also been shown to be influenced by the strain, but the half metallicity is preserved when the strain remains only moderate (from -4% to 4%) [20].

2.2 Magnetic anisotropy

The material specific exchange interaction can be seen as a far reaching conclusion of the Pauli exclusion principle, excluding electrons with the same spin from the same quantum state. This is also the origin of the long range magnetic ordering in ferro- and antiferromagnetic systems [40].

Although the exchange interaction can set the magnetic orientation ferro- or antiferromagnetic between two sublattices in a crystal, the exchange interaction alone does not picture the whole scenario of the magnetic alignment in macroscale samples. In order to talk about the direction of the magnetization in the lattice, magnetic anisotropy must be addressed. Anisotropy in general means that the properties are direction specific. Due to the magnetic anisotropy, the magnetic response of the material depends on the direction, for example on the direction between the magnetic field and the crystalline axes.

Ferro-, ferri and antiferromagnetic materials with the well-defined crystal axes exhibit magnetocrystalline anisotropy. This means that the spontaneous magnetization has a preferred orientation along a lattice vector. The phenomenon is rooted in spin-orbit interaction. In a crystal, the atomic orbitals, and therefore the electron motion, to some degree, can be considered being fixed to the crystalline directions. This happens because of the interaction between the orbital electrons and the potential, created by the other lattice atoms, stabilize the orbital to some crystal direction [40]. The exchange interaction sets the relative alignment between the adjacent spins. Due to the coupling between the spin angular momentum and the orbital angular momentum, all spins are coupled to the lattice. In a simplified phenomenological sense this gives rise to the magnetocrystalline anisotropy and to the magnetization easy and hard axes along the lattice vectors [41].

Magnetocrystalline anisotropy is important in any anisotropic system, where the exchange interaction and the spin orbit coupling set the relative orientation between the magnetic moments, with the well-defined directions for crystal axes. In the absence of a well-defined crystal axis, an isotropic system can still exhibit magnetization easy and hard axes. A magnetized ferromagnetic system creates a demagnetizing field opposing the field created by the magnetization. This field depends on the shape of the sample and demagnetizing field along one sample direction might differ from another. For example, a demagnetizing factor for an ideal thin film is nonzero only in parallel direction with the film plane normal [40]. Thin films, which are studied in this work, are a layer of material where in-plane area is roughly 4 mm$\times$4 mm and out-of-plane thickness

varies from tens to a couple of hundred nanometers. If a film was magnetized magnetic moment parallel to the film normal, a larger demagnetizing field would be created than when the magnetic moment parallel with the film plane [42, 43].

Magnetocrystalline anisotropy is linked to the crystal structure. Therefore, it is easy to guess, that any modification in the structure could also influence the orientation of the magnetic moment in the crystal. The phenomenon, where magnetization easy and hard axes are altered, because of the structural modification or stress, is called stress anisotropy or magnetoelastic anisotropy [40, 42].

Anisotropy results in an axis of equilibrium for the magnetic moment. The equilibrium and the magnetic moment can be influenced by the torque created by the magnetic field. By applying a magnetic field, work is done on the system and the magnetic moment can be moved away from the original equilibrium position, and from the easy axis, while a new equilibrium is created. The amount of work done per unit volume in order to reach the magnetization M can be expressed as

$$W = \int_0^M \mu_0 H dM, \tag{1}$$

where μ_0 is the magnetic permeability of free space, H is the magnetic field in the units of A/m and M is the magnetization [42]. The work done on the system is related to anisotropy constants. The direction of the magnetization can be divided into directional components expressed with direction cosines. The energy associated with the magnetocrystalline anisotropy is expressed as a power series of the directional components. The anisotropy constants are functions of coefficients from the power series expansion for the magnetocrystalline energy. For a cubic structure and symmetry, the magnetocrystalline energy density is written as follows

$$E_{crys} = K_0 + K_1(\alpha_1^2\alpha_2^2 + \alpha_1^2\alpha_3^2 + \alpha_2^2\alpha_3^2), \tag{2}$$

while neglecting higher order terms. Here $K_{\mathrm{i}=0,1}$ are the anisotropy constants and $\alpha_{i=1,2,3}$ are trigonometric terms obtained as presented in Figure 2. In principle, the anisotropy constants can be evaluated for a sample with the well-defined crystal directions by measuring the magnetization as a function of the magnetic field in different crystal directions [41, 42].

A qualitative understanding of the effects of anisotropy in real materials can be obtained by Stoner-Wohlfarth model. The model addresses uniformly magnetized particles where magnetization in the particle remains the same, but the direction of the magnetic moment can be changed. The model aims to minimize the total energy density of the system. The irreversible magnetization arises due to energy density exhibiting

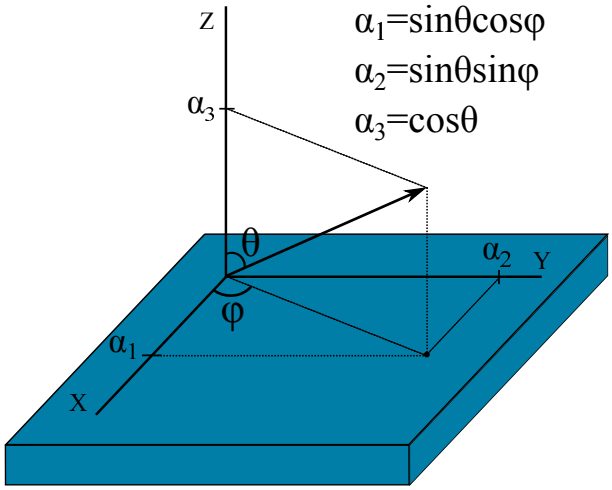

Figure 2. Schematic illustration of the magnetic moment, where axial components are characterized with the use of directional functions. These components can be used to describe the magnetocrystalline energy.

multiple minima. The irreversibility is influenced by the angle between the magnetization easy axis and the applied magnetic field. A larger angle results in smaller coercivity and remanent magnetization [40].

2.3 Magnetoresistance in multilayers and in complex oxides

Magnetoresistance in general refers to the change in resistance induced by the applied magnetic field acting on the system. This broad definition gives no restrictions on the source of the magnetoresistance and covers various phenomena with profoundly different origins. Mathematically magnetoresistance can be defined as

$$MR = \frac{R_{\mathrm{H}} - R_0}{R_0}, \tag{3}$$

where R_{H} refers to the resistance with an applied field H and R_0 refers to the resistance with a zero applied field.

The name giant magnetoresistance refers, in some sense, to the scale of the magnetoresistive response compared with the normal magnetoresistive signal. However, the phenomenon explicitly describes the magnetoresistive effect in multilayered systems, where the orientation of the relative magnetization in different ferromagnetic layers is either parallel or antiparallel. The phenomenon was first realized in Fe/Cr/Fe multilayers by P. Grünberg [44] and A. Fert [45].

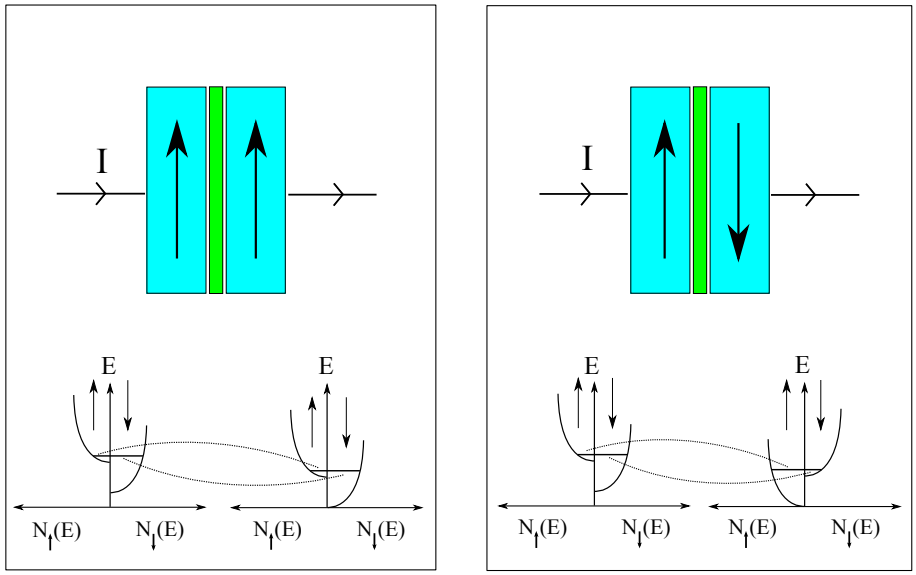

Figure 3. The spin-orbit splitting leads to unequal density of states between spin states in ferromagnetic materials. This is a source of resistance and in layered ferromagnetic structures resistivity of the system can be alterated with orientation of the magnetization between layers.

Giant magnetoresistance can be understood with the help of Mott's two current model [43, p. 261, 265]. Ferromagnetic materials can be considered having two polarized conduction bands, one for spin up and one for spin down electrons. When no spin-flip occurs, the conductivity of the system is essentially the sum of the conductivities in the two conduction bands. In other words, the two conduction bands can be considered as current channels connected parallel. Assuming a trilayer consisting of two identical ferromagnets, in respect to the band structure, and a nonmagnetic interface, parallel alignment and antiparallel alignment of the magnetization can result in the corresponding low and high resistivity states. The exchange splitting leads to different density of states in d-bands at the Fermi level in the ferromagnets. The resistivity of the channel and the scattering are proportional to the number of states available. Due to the exchange splitting, the density of states is different between two d-bands at the Fermi level. The parallel alignment leads to an out-come where the scattering in the other spin polarized band is higher and the other spin-band contributes only little to resistance. In the antiparallel alignment probability for the scattering is high in both spin channels [46].

The giant magnetoresistance phenomenon is by default an extrinsic property, where the transport properties are controlled with the relative magnetic orientation of the layers. Effectively similar kind of phenomenon is observed in magnetic tunnel junctions. However, in these systems the transport of electrons happens due to quantum mechanical tunneling. In a magnetic tunnel junction, two ferromagnetic layers are separated by an insulating layer. The relative orientation of the magnetic layers sets the device resistance high in the antiparallel orientation and low with the parallel orientation. Jullière's model explains the tunneling magnetoresistance as an alteration of conductance, based on the spin polarization of ferromagnetic materials. The well-known formulation for the spin-dependent tunneling is expressed with the equation

$$TMR = \frac{2P_1P_2}{1+P_1P_2}, \tag{4}$$

which relates the magnetoresistive effect to the spin polarizations of two ferromagnetic layers (P_1 and P_2) separated by an insulating layer. This formulation is a popular simplified characterization of the tunneling magnetoresistance phenomenon [47]. A schematic illustration of the tunneling scenario in a multilayered system with spin polarized ferromagnets is presented in Figure 3.

SFMO is quite often compared with colossal magnetoresistive manganites, partially due to the magnetoresistive properties. The colossal magnetoresistive manganite materials include such compounds as $La_{1-x}Sr_xMnO_3$, $La_{1-x}Ca_xMnO_3$ and $Pr_{1-x}Ca_xMnO_3$. Within the doping density ($0 < x < 1$), these materials have versatile magnetic phase diagrams. The variety of ordered states include ferromagnetic, antiferromagnetic and charge ordered states [48]. In a simplified sense, the understanding of the colossal magnetoresistance relies heavily on the argument about the competing co-existing insulating and metallic phases, enabling the material to go through an insulator-metal-transition, with an orders of magnitude shift in conductivity [49]. The magnetic field, needed for the phase transition, is in the order of teslas and basically outside of the application range.

The competition between the magnetic ground states, as seen in some of the manganite compounds, is not seen to be an important factor in SFMO considering the magnetoresistive properties [50]. Due to inter-grain tunneling between grain boundaries, of which magnetic orientation alter, the low field magnetoresistance (LFMR) phenomenon can take place. The applied magnetic field reduces the spin fluctuation between grains once the coercive field of the material is surpassed, lowering the resistance [53]. The LFMR effect happens usually within a much lower field range, around ± 0.1 T, when compared to the colossal magnetoresistance. In polycrystalline SFMO bulk samples the

LFMR, due to spin fluctuation between grains, is seen as the dominant contributor to magnetoresistance [1]. Since the epitaxial systems are by definition free of grain boundaries, where the relative orientation of grains alters in high angles, the magnetoresistive phenomenon due to inter-grain tunneling is suppressed in epitaxial films, with less structural defects [51]. The role of antiphase-boundaries are addressed being a vital factor in epitaxial SFMO thin films, regarding the magnetoresistance [51].

3 Experimental details

3.1 Thin film fabrication

Pulsed laser deposition (PLD) is a laser ablation method for thin film fabrication and has been successful in a complex oxide film deposition. A schematic illustration of the PLD setup is presented in Figure 4 (a). In order to deposit the film, high energy laser beam pulses are focused on a target material. The target material then vaporizes and the evaporated particles form a cloud of particles, usually referred to as "plume". A substrate material works as a base for the film. In proper deposition conditions the plume reaches the substrate and a stoichiometric deposition of the film can take place. A considerable advantage in the PLD is the adjustability of the deposition conditions. These include for example the choice of the substrate material, deposition temperature, laser fluence, pulse number, pulse frequency and deposition pressure. Like many complex oxides [54], SFMO thin films have been deposited using the PLD [15, 17, 19, 39, 55–59]. The effects of the deposition parameters on SFMO films have been a great focus in the studies.

All SFMO thin films in this work were prepared with the PLD. Before the film deposition, an appropriately chosen substrate was heated to a desired deposition temperature, between 900 °C–1050 °C (1173 K–1323 K), at the rate of 25 deg/min. The used substrate materials are listed in Table 2 in section 4.1.1. During the entire film preparation there was an adjusted background gas flow of Ar or Ar+$H_2$5% mixture. Once the deposition temperature was reached, the ablation was conducted using a XeCl eximer UV-laser. The wavelength of the laser radiation was 308 nm. The number of pulses during the laser ablation controls the thickness of the films. This work includes films fabricated with pulse numbers ranging from 500 to 10 000 pulses. After the ablation, the deposition temperature was maintained for 10 minutes, after which the temperature was decreased back to the ambient room temperature at the rate of 25 deg/min.

3.2 Surface characterization techniques

3.2.1 Atomic and magnetic force microscopy

Atomic force microscopy (AFM) is a high resolution scanning probe technique. A schematic illustration of the main components of the AFM setup is presented in Figure 4 (d). In AFM, a sharp nanometer scale tip, connected to a cantilever, works as a probe, which is brought in close proximity of the sample surface. Due to the short range forces,

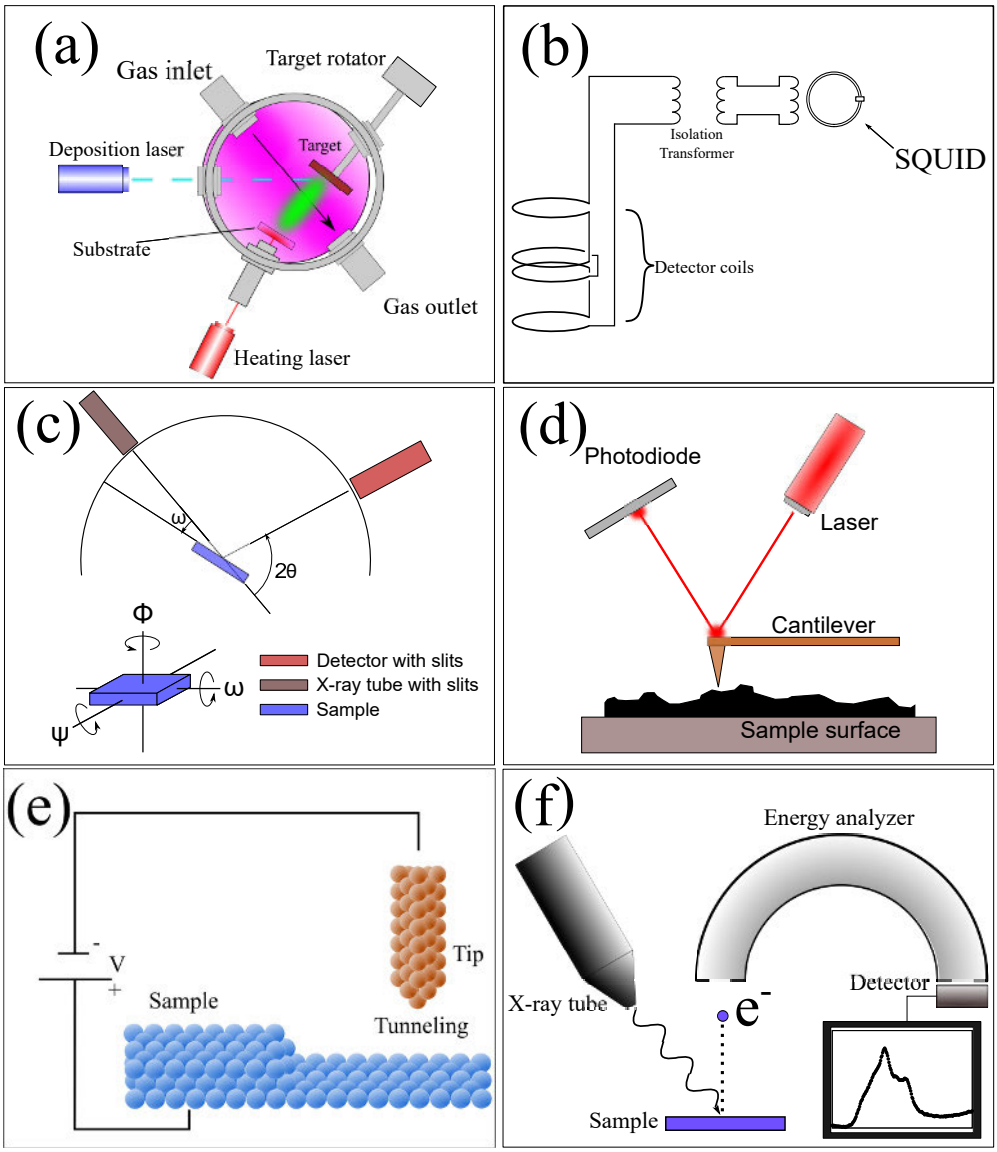

Figure 4. (a) A schematic illustration of a pulsed laser deposition setup. (b) A simplified reconstruction of the SQUID detection system as described in Quantum Design MPMS Hardware Reference Manual in more detail. (c) Geometry of the x-ray diffraction setup. (d) A schematic illustration of the principle behind the surface measurement with atomic force microscopy. (e) A schematic illustration of the principle behind the surface measurement with scanning tunneling microscopy. (f) An illustration of the x-ray photoelectron spectroscopy setup used in electronic surface analysis.

described by the Lennard-Jones potential, between the tip and the sample surface, the position of the tip is influenced by the sample topography. By scanning the sample surface, the surface structure can be recorded. An atomic force microscope can be operated in various modes: contact, tapping and non-contact mode. These modes allow the AFM measurements for more samples where another mode might be unusable. [60]

When the tip probe in AFM is lifted from the sample surface to for example 20 nm height, the short range forces have essentially no influence on the tip. The long range forces, including the electrostatic and the magnetic forces, are dominant with this distance. A silicon based AFM tip probe covered with a ferromagnetic coating can be used for detecting the magnetic long range forces. The electrostatic forces are also present in the magnetic signal and the quantitative interpretation of the data obtained with the magnetic force microscopy (MFM) may have to account for that.

The AFM measurements were conducted using Bruker Innova Atomic Force Microscope operating in contact mode and tapping mode. The root mean square (rms) roughness of a film was determined from 20×20 μm^2, 10×10 μm^2 and 5×5 μm^2 size AFM scans as an average obtained from various locations on the film surface. The corresponding MFM measurements were conducted with 25 nm, 50 nm, 100 nm and 200 nm lift heights. The magnetic tips used in the MFM and in the equivalent AFM measurements were Co-Cr coated silicon MESP-V2 tips provided by Bruker.

3.2.2 Scanning tunneling microscopy

The quantum mechanical tunneling effect can be harnessed as a microscopy technique for the surface characterization. This application is the scanning tunneling microscope (STM). In a system consisting of two electrodes separated by an insulating barrier, like vacuum, with an applied voltage between electrodes, electrons have a nonzero probability of tunneling through a potential barrier from one electrode to the other. Transport of an electron may take place even if electron's energy was smaller than the energy associated with the energy barrier. The tunneling current flowing through the potential barrier decays exponentially with increasing barrier width. In the low voltage regime the tunneling current density is proportional to the separation z between two conductive electrodes

$$J \propto \frac{V}{z} e^{-2\kappa z}, \tag{5}$$

where V is the applied voltage, ρ_S the local density of states, κ the decay constant [61]. In the high voltage regime, the representation of the current becomes more complex. This relation provides an extremely sensitive method for the characterization of the

surface structures. The tunneling however is not only influenced by the surface structure but also by the changes in the local density of states [62].

The used STM setup was OMICRON Fermi SPM ultra high vacuum scanning probe microscope. During the measurements included in this work, the sample temperature was set to 84 K using liquid nitrogen. The aim was to achieve a greater thermal stability and therefore a higher resolution. The low-temperature STM setup somewhat resembles the AFM setup used in this work. A tip, with the head size of atomic scale, is brought in close proximity with the sample surface enabling the tunneling phenomenon. With xyz-piezo-tubes the sample surface is scanned and the topography of the sample surface is reconstructed. A schematic illustration of the working principle of the STM setup is presented in Figure 4 (e).

3.2.3 X-ray photoelectron spectroscopy

An inelastic collision between an electron and an x-ray photon can be harnessed as a spectroscopic technique to learn about the electronic structure of the material. The method known as x-ray photoelectron spectroscopy (XPS), also known as electron spectroscopy for chemical analysis (ESCA), is a method where an electron is excited and eventually ejected from the material. This is achieved by providing the electron with additional energy with the use of a high energy photon [63]. An electron is bound to its state by the specific binding energy. A sufficient amount of energy received from the photon is enough for the material to emit an electron with the low enough binding energy and a part of the energy revived from the photon goes to kinetic energy of the electron. The relation between the photon energy and the kinetic energy of an electron can be described as

$$E_{\text{kin}} = E_{\text{photon}} - E_{\text{B.E}} - \Phi. \tag{6}$$

The photon energy, E_{photon}, is therefore consumed to the kinetic energy E_{kin}, to overcome the binding energy $E_{\text{B.E.}}$ and the instrumental work function Φ. A schematic illustration of the working principle of the XPS setup is presented in Figure 4 (f).

In this work, the conventional laboratory x-ray photoelectron spectroscopy measurements were done in ultra high vacuum with Perkin-Elmer PHI 5400 using Mg Kα (1253.6 eV) x-ray radiation with the pass energy of 35 eV. C 1s (284.8 eV) was used as a standard for the binding energy calibration. The quantitative analysis of the XPS spectra was conducted by identifying the sum of different valence states with pseudo-Voigt profiles combined with a Shirley type background. Fitting was performed using

the SPANCF curve fitting macro package, as presented in [73, 74] using Igor Pro fitting program.

3.3 Diffraction measurements

The structural characterization of the crystal lattice can be largely credited for x-ray diffraction (XRD) techniques. The diffraction of x-rays from the lattice site elements and the repetitive periodical structure of the crystal results in conditional constructive interference. This relates the crystal structure and the measurement setup with the relation to the constructive interference described geometrically by Bragg's law

$$n\lambda = 2d\sin(\theta). \tag{7}$$

The equation joins the distance d between the lattice planes to the coherent wave length λ and to the angle θ between the incoming radiation and the lattice plane. No limitation is set for possible lattice planes producing the interference. However, due to structural factors in the lattice some of the interference patterns, predicted by Bragg's law, in the resulting diffractogram may even die out [64].

A schematic illustration of the working principle of the x-ray diffraction setup is presented in Figure 4 (c). There were two different x-ray diffractometers used in this work, Philips X'Pert Pro MPD diffractometer with Schulz goniometer and Empyrean diffractometer with five axis goniometer, both with Cu Kα radiation. The measurement

Table 1. Details of the x-ray diffraction setup parameters used in Philips X'Pert Pro MPD and in Empyrean diffractometer.

Diffractometer	Philips X'Pert Pro MPD	Empyrean diffractometer
X-ray tube	Empyrean Cu LFF 40 kV 45 mA	Empyrean Cu LFF HR 45 kV 40 mA
Soller slit	0.04 rad $\times 2$	0.02 rad $\times 2$
Filter	Nickel	BraggHD monochromator
Divergence Slits	1/4°	1/2° & 1/4°
Mask	10 mm	4 mm
Antiscatter Slit	7.5 mm	7.5 mm
Goniometer	Schulz	Five axis
Detector	PIXcel1D/	PIXcel3D

configurations are listed in Table 1. $\theta - 2\theta$ measurements in $(00l)$ orientation, covering at least the range of $20^\circ - 110^\circ$, were conducted to confirm the phase purity of the films and were also used in calculating SFMO lattice *c*-parameter. For a more accurate impurity phase check, $\phi - \Psi$ scans were performed for the possible impurity phases including Fe (110) ($2\theta = 44.98^\circ$) and $SrMoO_4$ (112) ($2\theta = 27.68^\circ$). $\phi - \Psi$ and $2\theta - \phi$ scans were performed on SFMO (204) peak ($2\theta = 57.106^\circ$) for the texture and the low angle grain boundary analysis, respectively.

3.4 Magnetometry

A superconducting quantum interference device magnetometer, also known as SQUID magnetometer, was used to measure the magnetic properties of SFMO films. The SQUID setup, used in this work, was a commercial Quantum Design MPMS radio frequency SQUID magnetometer. A special component in a SQUID magnetometer is the superconductive loop including a Josephson junction. This junction is, through other circuitry, inductively connected to detector coils. Once the sample moves through the detector coils, the magnetic flux through the detector coils is altered. Change in the magnetic flux has a response in the electrical current running through the detector coils according to Lenz's law. This response is then measured with the SQUID and by comparing the signal to a standardized counterpart, the magnetic moment of the sample is reconstructed. A simplified reconstruction of the SQUID detection system as described in Quantum Design MPMS Hardware Reference Manual is presented in Figure 4 (b).

The measurements include zero field cooled (ZFC) and field cooled (FC) magnetization, or magnetic moment, as a function of temperature in a constant magnetic field. Magnetization hysteresis loops were recorded between ± 0.5 T in other measurements except while studying anisotropy, when the loops were obtained between ± 1 T. The temperature during a single hysteresis measurement was kept constant and several measurements were obtained at various temperatures between 10 K and 400 K.

3.5 Magneto-transport measurements

Magneto-transport measurements for SFMO based spin valve devices and respective SFMO layer were measured using Quantum Design Physical Property Measurement System (PPMS). The measurements were done with resistivity option using four-point measurements. A schematic illustration of the measurement setup for SFMO/Alq_3/Co/Al junction is presented in Figure 5. The relevant measurements were done by applying 50 nA constant current and include the resistive measurements at 10 K, 100 K, 200 K

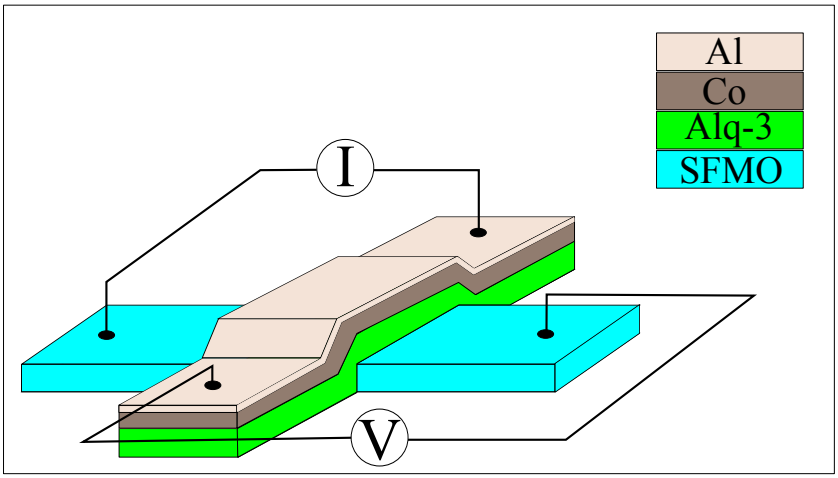

Figure 5. A schematic illustration of SFMO spin valve where transport layer is organic Alq_3. Ferromagnetic Co layer is protected with Al layer **[P7]**.

and 300 K temperatures. The field range applied in these measurements was between -500 mT and +500 mT. The magnetic field was applied in the film plane along SFMO (110) lattice vector direction.

4 Results for Sr_2FeMoO_6 thin film characterization

4.1 Thin film bulk investigations

Literature usually identifies bulk samples as polycrystalline powder samples although sometimes bulk is used to distinguish the film properties from the surface properties. In the absence of a better label, bulk investigation in the following chapters refers essentially to the techniques, where measurement results from the films arise from the entire sample volume and no separation between the surface and the rest of the film (bulk) can be made reliably. X-ray diffraction measurements provide microstructural information, including e.g. the lattice structure and micro distortion in it, beyond the sample surface, which relates to the magnetic properties. Magnetometric measurements are profoundly important for the sample quality monitoring. The value of SFMO is partially due to possible spin valve operation at room temperature, which is due to the high ferri−paramagnetic transition temperature, maintaining spin polarization at high temperatures, possibly exceeding room temperature. For partially this reason, Curie temperatures were measured for all our samples. For a more thorough magnetic analysis, M_{sat}, magnetization irreversibility (M_{irr}) and coercive field (B_{c}) were also determined.

4.1.1 Lattice structure

The film deposition essentially results with a flawed single crystal system. The level of distortion is a valid research area, which can be approached using XRD techniques. All the included samples measured with XRD are thin films. A schematic illustration of SFMO unit cell, grown on STO substrate, is presented in Figure 6. The coordinate system in Figure 6 is set according to STO unit cell. The only exception is the reported results for the polycrystalline powder pellet sample, used as a target during the PLD deposition **[P2]**. The XRD results, for the target pellet, depicted an outcome expected for a polycrystalline phase pure SFMO sample. An example of $\theta - 2\theta$ measurement results for films is obtained from **[P2]** and presented here in Figure 7 (a). The constructive interference occurs only for some of the peaks. The peaks, which give rise to diffraction peaks, are identified as $(00l)$ peaks. The absence of the peaks, outside of the $(00l)$ group, suggests that the films are c-axis oriented, meaning in this case that c axis is perpendicular with the film plane. $\Phi - \psi$ measurements, or the texture measurements, were conducted for (204) SFMO peak with $2\theta = 57.106^{\circ}$. An example of the results is provided in Figure 7 (b). The results show peaks arising from the (204) and (132) peaks, as expected for a fully texturized SFMO lattice. In conclusion, indeed all

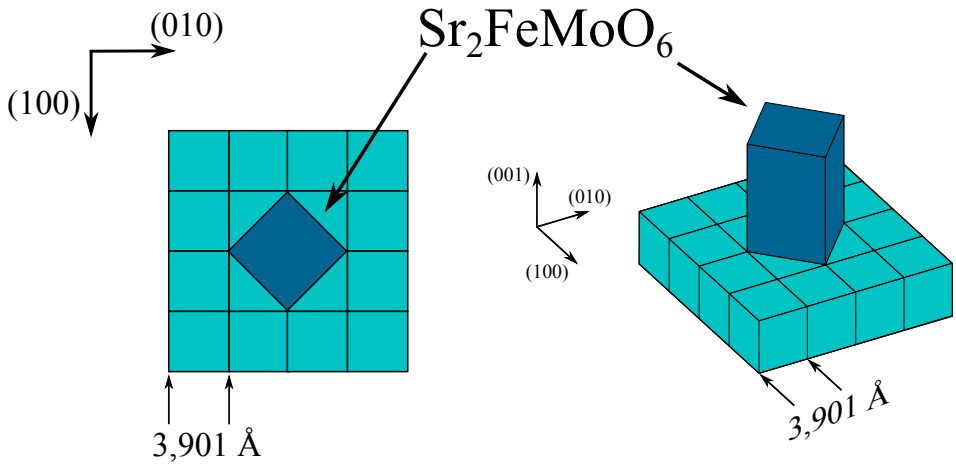

Figure 6. A schematic illustration of SFMO unit cell (dark blue) grown on STO substrate (light blue). The coordinate system shows the lattice directions for STO substrate.

the films included in this work are fully texturized and *c* axis oriented.

X-ray diffraction was the premier technique for the lattice structure and the impurity analysis. In this work, most of the analysis showed no evidence of impurity traces in the XRD characterization. As an exception, a possible trace of $SrMoO_4$ phase was observed in two of the samples in **[P2]**, where the effect of the laser fluence during the film deposition was investigated. The impurity trace was realized both in $\theta - 2\theta$ measurements, and in complementary $\Phi - \psi$ measurements conducted for $SrMoO_4$ (112) with $2\theta = 27.680°$, presented in Figure 7 (c). It was suggested, that the nonoptimal film deposition conditions might cause the formation of the impurity phase. This would mean an inappropriate laser fluence. However, a small amount of impurity phase, below the XRD detection limit, could also exist in the target material used in the deposition, which could then transfer the impurity phase to the film. All the films were also checked for metallic Fe impurities by measuring $\Phi - \psi$ Fe (110) with $2\theta = 44.980°$. However, no trace of Fe impurity was detected (see Figure 7 (d)). The argument for the impurity free SFMO films is valid within XRD detection limit of 1% of total film volume.

The analysis of SFMO lattice constants begins by identifying SFMO diffraction peaks with the correct Miller indices (hkl). The Miller indices define a plane in the real lattice space, where the separation between the two nearest planes can be presented as a function of the lattice constants and the Miller indices for an orthorombic system as follows

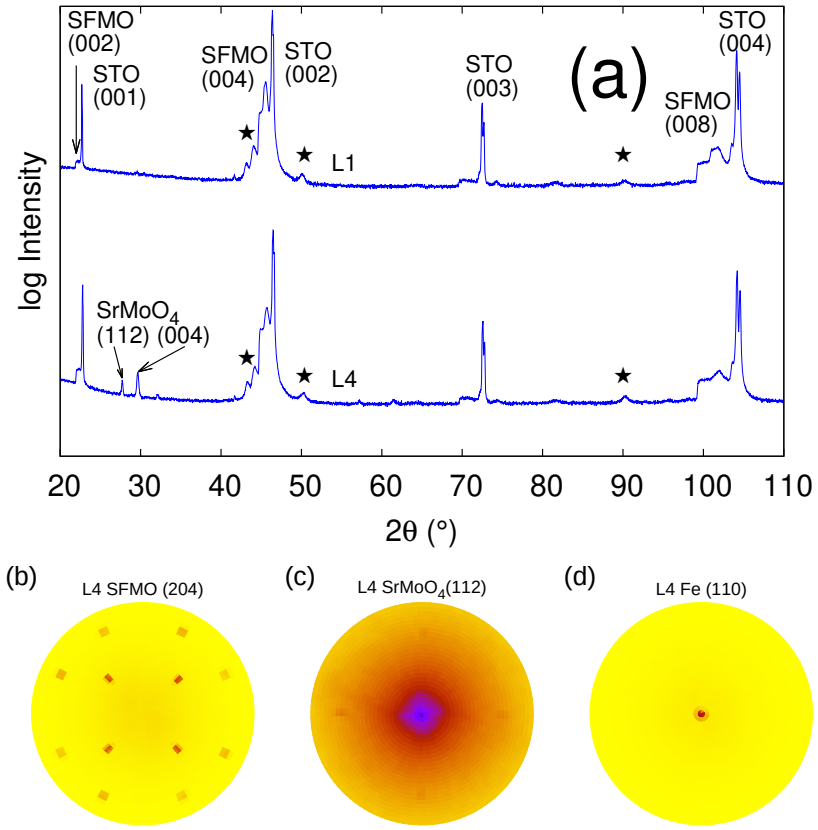

Figure 7. (a) An example of the $\theta - 2\theta$ results, both for a impurity-free SFMO thin film sample and for a SFMO film containing $SrMoO_4$ impurity phase. The results show $(00l)$ peaks for SFMO and STO substrate and impurity peaks identified as peaks arising from (112) and (004) planes. The peaks arising from the sample holder are labeled with the symbol ★. (b), (c) and (d) present the results obtained with $\Phi - \psi$ results for impurity rich SFMO film for SFMO (204), $SrMoO_4$ (112) and Fe (110), respectively **[P2]**.

$$\frac{1}{d^2} = \frac{h^2}{a^2} + \frac{k^2}{b^2} + \frac{l^2}{c^2}. \tag{8}$$

This simplifies for the tetragonal SFMO lattice, since $a = b$. From the peaks identified as $(00l)$ peaks, the c parameter can be calculated. In **[P1]** the evaluation was made by characterizing $(00l)$ diffraction peaks as the sum of two Gaussian functions, one for $K_{\alpha 1}$ and for $K_{\alpha 2}$, and using the Nelson-Riley method. In**[P3]** the evaluation was made by characterizing a single $(00l)$ diffraction peak as the sum of two Gaussian functions.

In **[P2]**, pseudo-Voigt profiles were used. Once the c parameter is evaluated, $a = b$ parameter can be determined from the peaks with $h \neq 0$ and/or $k \neq 0$.

The lattice parameter values depend strongly on the chosen substrate material used in the film fabrication. The lattice mismatch between the substrate and SFMO induces structural stress, creating elongation and/or contraction to SFMO lattice. The used substrates in this work including $SrTiO_3$, $(LaAlO_3)_{0.3}(Sr_2AlTaO_6)_{0.7}$ (LSAT) and $SrLaAlO_4$ (SLAO) single crystal substrates, with lattice mismatches of -1.05%, -1.88% and -4.73%, respectively, are listed in Table 2. The lattice mismatch is calculated from the diagonal of the (001) plane of the single substrate unit cell, according to $\eta = \frac{\sqrt{2}a_{\mathrm{STO}} - a_{\mathrm{SFMO}}}{a_{\mathrm{SFMO}}}$. This is because SFMO crystal orients itself a/b parameter on the diagonal of the (001) plane, along the [110] lattice vector of the substrate, once the substrate (001) plane is an available growth site. This minimizes the lattice mismatch between the substrate and SFMO. A negative lattice mismatch could be thought to imply compressive stress for a and b parameters. Assuming a positive Poisson's ratio, this would lead to an elongation in c parameter. Table 3 lists the obtained strain values from the projects included in this work. The strain values range from -0.13% to $+0.94\%$ in c parameter (ε_{c}) and from -0.86% to $+0.46\%$ in a parameter (ε_{a}). The strain seems to be heavily influenced, at least, by the lattice mismatch between the substrate material and SFMO and by the film thickness. The reported strain values for the SFMO films fabricated on STO, show tensile ε_{c} values and compressive ε_{a} values. These films also show the largest absolute values for both ε_{c} and ε_{a} lattice strain. The films grown on SLAO and LSAT substrates showed an elongated lattice along a axis. At the same time, the films grown on SLAO and LSAT showed compressive and mostly tensile strain along c axis, respectively.

The origin of the strain particularly arises from the substrate material. Once the

Table 2. The substrates used in this work, with their lattice constants and mismatches between SFMO and the substrate. The lattice parameter refers to a parameter for all the substrates.

Substrate	Lattice constant a (Å)	Mismatch (%)
$SrTiO_3$	3.901	-1.05
$(LaAlO_3)_{0.3}(Sr_2AlTaO_6)_{0.7}$	3.868	-1.88
$SrLaAlO_4$	3.756	-4.73

Table 3. SFMO films used in this work are listed with used substrate material and structural results including $(008)\Delta 2\theta$, $(204)\Delta\Phi$, $(101)\Delta\Phi$, $(004)\ \Delta\omega$, ε_a and ε_c **[P1], [P2], [P3], [P4], [P5], [P6]**.

Sample	Substrate	$(008)\Delta 2\theta/(^\circ)$	$(204)\Delta\Phi/(^\circ)$	$(101)\Delta\Phi/(^\circ)$	$(004)\Delta\omega/(^\circ)$	$\varepsilon_a(\%)$	$\varepsilon_c(\%)$
STO 40	$SrTiO_3$	-	-	-	-	-0.45	0.52
STO 80	$SrTiO_3$	-	-	-	-	-0.79	0.93
STO 120	$SrTiO_3$	-	-	-	-	-0.85	0.94
STO 160	$SrTiO_3$	-	-	-	-	-0.71	0.78
STO 400	$SrTiO_3$	-	-	-	-	-0.12	0.41
STO 800	$SrTiO_3$	-	-	-	-	-0.26	0.05
LSAT 35	$(LaAlO_3)_{0.3}(Sr_2AlTaO_6)_{0.7}$	-	-	-	-	0.35	0.020
LSAT 70	$(LaAlO_3)_{0.3}(Sr_2AlTaO_6)_{0.7}$	-	-	-	-	0.29	0.063
LSAT 105	$(LaAlO_3)_{0.3}(Sr_2AlTaO_6)_{0.7}$	-	-	-	-	0.36	0.057
LSAT 140	$(LaAlO_3)_{0.3}(Sr_2AlTaO_6)_{0.7}$	-	-	-	-	0.26	0.012
LSAT 350	$(LaAlO_3)_{0.3}(Sr_2AlTaO_6)_{0.7}$	-	-	-	-	0.46	-0.054
LSAT 700	$(LaAlO_3)_{0.3}(Sr_2AlTaO_6)_{0.7}$	-	-	-	-	0.38	0.012
L1	$SrTiO_3$	1.63	-	-	-		+0.56
L2	$SrTiO_3$	2.15	-	-	-		+0.43
L3/T1	$SrTiO_3$	0.55	-	-	-		+0.56
L4	$SrTiO_3$	1.17	-	-	-		+0.59
T2	$SrTiO_3$	0.72	-	-	-		+0.70
T3	$SrTiO_3$	0.64	-	-	-		+0.61
T4	$SrTiO_3$	1.79	-	-	-		+0.56
X1	$SrTiO_3$	1.43	-	-	-		+0.62
STO-1	$SrTiO_3$	-	-	-	-	-0.86	+0.90
STO-2	$SrTiO_3$	-	0.692	-	-	-0.46	+0.60
SLAO-1	$SrLaAlO_4$	-	1.013	-	-	+0.05	-0.13
SLAO-2	$SrLaAlO_4$	-	0.914	-	-	+0.03	-0.11
S-500	$SrTiO_3$ (Nb doped)	-	-	-	-	-	-
S-2000	$SrTiO_3$ (Nb doped)	-	-	-	-	-	-
A1	$SrTiO_3$	-	0.467	0.481	0.243	-	-
A2	$SrTiO_3$	-	0.692	0.970	0.535	-	-
AH1	$SrTiO_3$	-	0.573	0.654	0.295	-	-
AH2	$SrTiO_3$	-	0.830	1.204	0.521	-	-
T25	$SrTiO_3$	-	-	-	-	-	-
T200	$SrTiO_3$	-	-	-	-	-	-
T400	$SrTiO_3$	-	-	-	-	-	-
T550	$SrTiO_3$	-	-	-	-	-	-

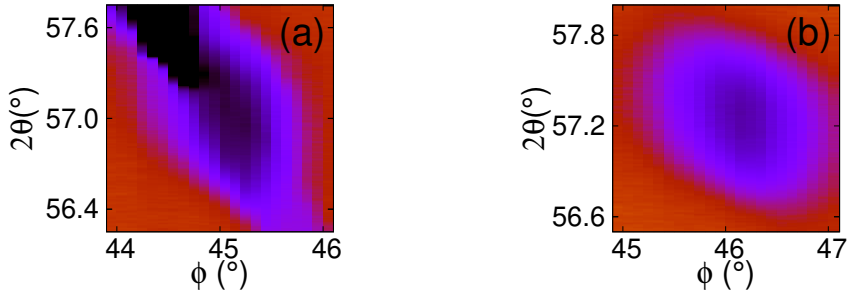

Figure 8. $2\theta - \Phi$ measurement results for SFMO (204) peak. Films are deposited on (a) STO and (b) SLAO. The diffraction results for SFMO on STO are clearly influenced by the overlapping STO peak, while there is no a significant overlap between SLAO and SFMO **[P3]**.

film deposition takes place, the first SFMO layers become under compressive or tensile strain, depending on the substrate. When the film thickness is increased, the lattice parameters tend to become relaxed towards the bulk values. The strain and other mismatch related structural defects and their influences are therefore usually more dominant in thinner films. The structural analysis in this work for the strain is in partial agreement with this, with exceptions. In **[P3]** smaller strain values were obtained when thicker films were fabricated. Similar conclusions were drawn in **[P1]**. However, the strain relaxation with increasing film thickness was not completely clear. While all the substrates included in this work exhibit negative a/b lattice mismatch, compared with SFMO, negative and positive strain values were obtained. It would seem that the SFMO films, deposited on LSAT and SLAO, experience an over-relaxation or relaxation, resulting in positive in-plane strain values. Considering the strain values, obtained in other research projects, the correlation, between compressive or elongated lattice mismatch and respectively compressive or elongated strain, is not always clear. However, similar results depicting elongated c parameter strain (ε_c) and/or compressive a parameter strain (ε_a) in SFMO films on STO have been reported [10, 39, 65–67]. The over-relaxation has also been reported for SFMO films with compressive in-plane mismatch with the substrate [10, 67].

Besides the strain analysis, the broadening in the diffraction peaks was also analyzed. The full width at half maximum (FWHM), indicated with Δ, values were obtained from the peak characterization parameters and used to describe the broadening

of the XRD peaks. The broadening of the diffraction in Φ angle was analyzed in $\Phi - 2\theta$ results for (204) in **[P3]** and **[P5]** and for (101) in **[P5]**. Figure 8 presents the results obtained for $\Phi - 2\theta$ results for (204) in **[P3]**. In **[P2]**, the $2\theta-$broadening was analyzed for SFMO (008) peaks. The results are listed in Table 3. The broadening in part tells about the structural deviation from the ideal single crystal structure, like stacking faults, low angle grain boundaries or tilts in the lattice planes. Although also instrumental imperfections cause peak broadening. The structural analysis would indicate that the structural faults are in large part linked to the film deposition conditions. The relevant parameters at least include the gas flow and the choice for the substrate material. Higher Ar and Ar+$H_2$5% gas flow during the deposition seems to result in more structural deviation, when compared with the low gas flow, in all included analysis areas **[P5]**. $\Delta\Phi$ broadening showed an increase from $0.481^\circ - 0.654^\circ$ to $0.970^\circ - 1.204^\circ$ in (101) SFMO peak and an increase from $0.467^\circ - 0.573^\circ$ to $0.692^\circ - 0.830^\circ$ in SFMO (204) peak, when the higher gas flow was used during the deposition. This describes the rotational tilt in the unit cells along the plane normal vector. In addition, $\Delta\omega$ broadening in (004) peak showed an increase from $0.243^\circ - 0.295^\circ$ to $0.535^\circ - 0.521^\circ$ **[P5]**. This describes for example a tilt in c parameter from the film plane normal. The films deposited on SLAO substrate, with larger lattice mismatch with SFMO bulk, when compared with the mismatch between STO and SFMO, showed larger $\Delta\Phi$ values in (204) peak, from 0.914° to 1.013° on SLAO and 0.692° on STO, associated with low angle grain boundaries in the films **[P3]**. In addition, in **[P2]**, the lower deposition temperature resulted in greater $\Delta 2\theta$ values. Laser fluence was also seen to have an apparent effect on the diffraction broadening, which could, however, be due to impurity defects, causing distortion in the phase pure SFMO lattice.

The results for the structural characterization have so far suggested that the SFMO films become altered from the ideal crystalline structure. The sources for more systematic structural deviation at least include the lattice mismatch between the substrate and SFMO and the gas flow rate. Higher flow rate resulted in more structural faults and the mismatch between the substrate and the film resulted in lattice strain. It is fair to ask what is the accuracy of the structural analysis. The obtained information is derived from the peak fitting. The applied software for peak fitting in most cases was Gnuplot. The software utilizes a non-linear least square fitting. The error in fitting parameters, like in the peak position and broadening, is provided as an absolute standard error. As an illustration, the fitting of Gaussian function with Gnuplot for (008) SFMO peak results in an asymptotic standard error of approximately $\pm 0.002^\circ$ in the peak position in

2θ. Considering the effect on c lattice parameter, this would roughly result in a deviation of 0.08% in the absolute lattice parameter. This example suggests that the smallest differences in strain values are within the error limits, meaning that for example the differences in strain between the SFMO samples deposited on SLAO substrates become indistinguishable. This is reasonable. The error value for the illustration was obtained with $\theta - 2\theta$ measurement results for SLAO-2 sample. Similar error values in the ε_c in the 700 nm thick SFMO film deposited on LSAT, suggest that the ε_c values might represent relaxation rather than over-relaxation of the film lattice.

4.1.2 Magnetic characterization

The wide interest towards SFMO in the near history has profoundly risen due to the high spin-polarization, resulting in the magnetoresistive phenomenon, combined with the exceptionally high T_C. These attributes are of particular importance for the fundamental research and the application point of view. The influence of the lattice site augmentation on the properties of SFMO is well addressed in the other peer reviewed articles and the evidence points mainly to the loss of spin-polarization [26], decrease of saturation magnetization [23, 26, 68] and decrease of T_C [27, 68] with an increased amount of ASD in the Fe and Mo sites. Although the effects on the T_C seem somewhat more versatile, since in high enough concentrations the ASD could also increase the T_C [13]. The effect of oxygen vacancies is not well established, in both theoretical and experimental studies. Based on the current understanding, oxygen vacancies result in higher T_C and with lower M_{sat}, while maintaining the spin polarization, at least in low concentrations [13, 14, 31]. In addition to the mis-site and the vacancy defects, the samples are influenced by the low angle grain boundaries, strain and impurities.

The magnetic bulk investigations included in this work are conducted exclusively with SQUID magnetometer. The effects of the film deposition parameters were investigated by studying the magnetic properties of the films, which were fabricated with different laser fluence during ablation, at various deposition temperatures, with different pulse numbers, in different gas atmospheres and on different substrate materials. As an example, Figure 9 (a) presents the results for ZFC/FC magnetizations obtained in **[P6]**, with the first order derivative of FC magnetization in the inset of Figure 9 (a). The results depict a common decay of magnetization with increasing temperature. A clear ferri−paramagnetic transition is observed between 314 K and 351 K, as the annealed sample shows an increase in T_C. An example of the magnetization hysteresis measurement results is presented in Figure 9 (b) **[P6]**. Most of the obtained results for SFMO films showed a similar outcome of saturated magnetization in high fields along with remanence and coercivity. A quantitative analysis provides a clearer distinction between the samples. The samples differ in the lattice mismatch between the film and the substrate, thickness of the films, laser fluence during the deposition ablation, deposition temperature, gas flow and *ex-situ* annealing. Their influence on the magnetic properties are discussed in the following paragraphs. For illustration, the combined results for T_C, M_{sat}, M_{irr} and B_c are presented in Figures 9 (c)-(f) and listed in Table 4. The apparent variation in the results is in part due to the internal film deposition parameter variation within each study. For a direct comparison and conclusions between the different pub-

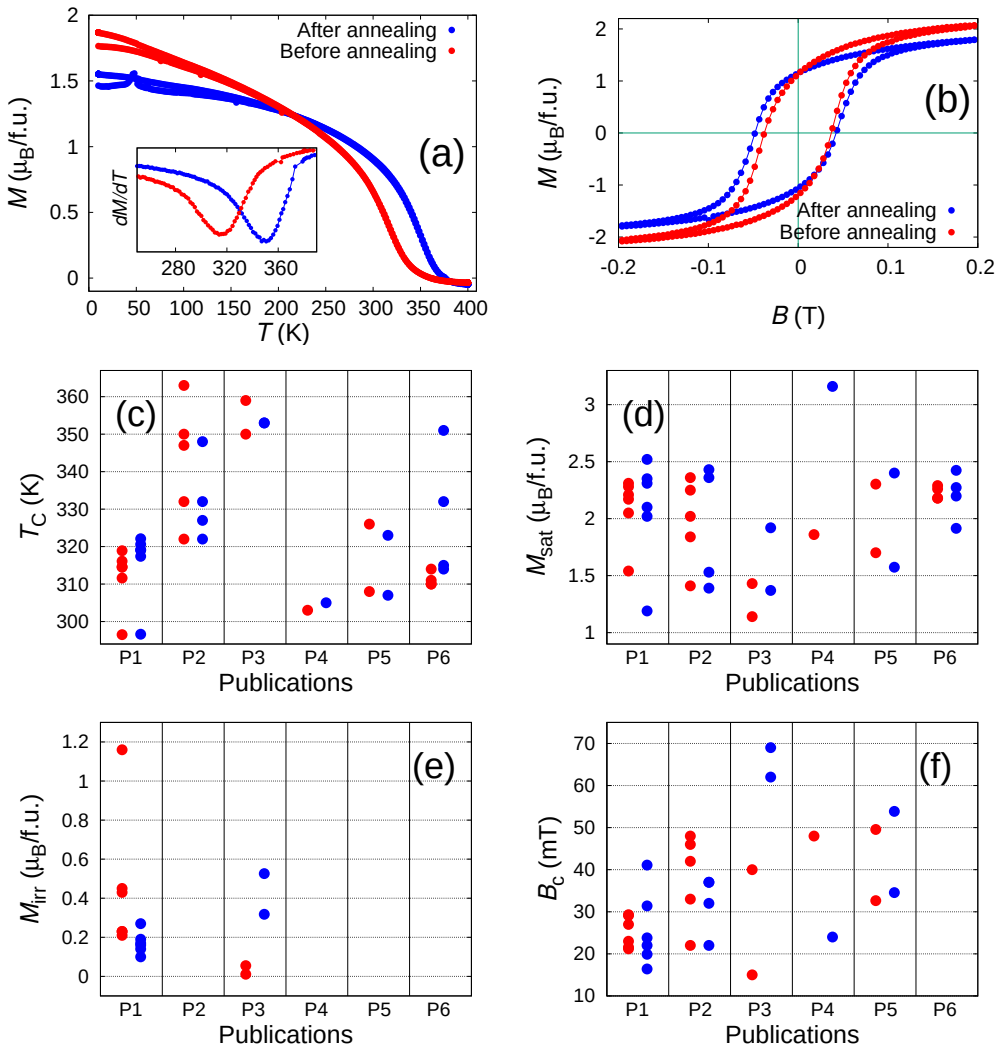

Figure 9. An example of the ZFC/FC measurements (a) between 10 K and 400 K in 100 mT field along with the magnetic hysteresis measurements (b) at 10 K between ±500mT **[P6]**. Grouped results from the included publications including T_C (c), M_{sat} (d), M_{irr} (e) and B_c (f). The colors refer to the parameters used in the film deposition in the research project (red/blue: **[P1]** STO/LSAT substrate, **[P2]** temperature/laser fluence, **[P3]** STO/SLAO substrate, **[P4]** 500 laser pulses/2000 laser pulses,**[P5]** Ar/Ar+$H_2$5% deposition gas, **[P6]** before/after the annealing). Original publications should be viewed before detailed comparisons are made between the results.

Table 4. SFMO films used in this work are listed with used substrate material, deposition temperature and magnetic results including T_C, M_{irr}, M_{sat} and B_c **[P1], [P2], [P3], [P4], [P5], [P6]**.

Sample	Substrate	T_d	T_C/(K)	$M_{irr}/(\mu_B/\text{f.u.})$	$M_{sat}/(\mu_B/\text{f.u.})$	B_c/(mT)
STO 40	$SrTiO_3$	1050 °C	297	1.16	1.54	29.1
STO 80	$SrTiO_3$	1050 °C	315	0.45	2.05	29.3
STO 120	$SrTiO_3$	1050 °C	312	0.43	2.21	27.0
STO 160	$SrTiO_3$	1050 °C	319	0.23	2.17	23.0
STO 400	$SrTiO_3$	1050 °C	315	0.21	2.31	21.2
STO 800	$SrTiO_3$	1050 °C	316	0.23	2.28	21.6
LSAT 35	$(LaAlO_3)_{0.3}(Sr_2AlTaO_6)_{0.7}$	1050 °C	297	0.19	1.19	41.1
LSAT 70	$(LaAlO_3)_{0.3}(Sr_2AlTaO_6)_{0.7}$	1050 °C	319	0.27	2.02	31.4
LSAT 105	$(LaAlO_3)_{0.3}(Sr_2AlTaO_6)_{0.7}$	1050 °C	321	0.14	2.10	23.75
LSAT 140	$(LaAlO_3)_{0.3}(Sr_2AlTaO_6)_{0.7}$	1050 °C	322	0.10	2.31	22.0
LSAT 350	$(LaAlO_3)_{0.3}(Sr_2AlTaO_6)_{0.7}$	1050 °C	317	0.17	2.35	19.9
LSAT 700	$(LaAlO_3)_{0.3}(Sr_2AlTaO_6)_{0.7}$	1050 °C	319	0.16	2.52	16.4
L1	$SrTiO_3$	1050 °C	327	-	2.43	37
L2	$SrTiO_3$	1050 °C	348	-	1.53	37
L3/T1	$SrTiO_3$	1050 °C	322	-	2.36	22
L4	$SrTiO_3$	1050 °C	332	-	1.39	32
T2	$SrTiO_3$	1000 °C	332	-	1.84	33
T3	$SrTiO_3$	950 °C	347	-	2.25	42
T4	$SrTiO_3$	900 °C	350	-	2.02	48
X1	$SrTiO_3$	900 °C	363	-	1.41	46
STO-1	$SrTiO_3$	900 °C	350	0.011	1.14	40
STO-2	$SrTiO_3$	900 °C	359	0.055	1.43	15
SLAO-1	$SrLaAlO_4$	900 °C	353	0.318	1.37	69
SLAO-2	$SrLaAlO_4$	900 °C	353	0.526	1.92	62
S-500	$SrTiO_3$ (Nb doped)	1050 °C	303	-	1.86	48
S-2000	$SrTiO_3$ (Nb doped)	1050 °C	305	-	3.16	24
A1	$SrTiO_3$	1050 °C	308	-	2.303	32.65
A2	$SrTiO_3$	1050 °C	326	-	1.701	49.55
AH1	$SrTiO_3$	1050 °C	307	-	2.400	34.55
AH2	$SrTiO_3$	1050 °C	323	-	1.574	53.85
T25	$SrTiO_3$	1050 °C	314	-	2.273	-
T200	$SrTiO_3$	1050 °C	315	-	2.424	-
T400	$SrTiO_3$	1050 °C	332	-	2.198	-
T550	$SrTiO_3$	1050 °C	351	-	1.915	-

lications, readers are encouraged to first carefully consider the differences between the deposition conditions. However, most of the presented values are quite well within the range of previous publications [10, 13]. As an example, the high B_c in Figure 9 (f) in **[P3]**, compared to a previous result [10], is likely due to the combined effect of magnetic anisotropy and defect induced domain pinning. All the T_C values are close to room temperature or are considerably higher. These issues are discussed further in this work.

The lattice mismatch was induced by the use of the various substrate materials in SFMO film deposition. The substrate materials used in the thin film deposition are as listed in Table 2. In **[P1]**, the films were deposited on LSAT and STO substrates with various thicknesses. The effect of the film thickness appears with the results, suggesting that the thinner films have a higher concentration of structural defects induced by the substrate, which influence the magnetic properties by decreasing T_C and saturation magnetization. T_C ranges from the lowest 297 K to the highest values of 319 K and 322 K, respectively for the SFMO films on STO and LSAT. Domain pinning is stronger in thinner films on both substrates, as shown by the higher B_c and M_{irr} at low temperatures between ZFC and FC magnetization. Once the film thickness reaches approximately 100 nm, magnetic properties remain essentially unaffected by the increase in thin film thickness. In **[P4]**, the B_c and M_{sat} were respectively higher and lower in the thinner film compared with the thicker film. This provides additional evidence for substrate induced defects in SFMO films. However, the T_C remained in this case largely unaffected. The results seem to suggest that higher lattice mismatch induces more structural defects, giving rise to stronger domain pinning. This was rather clear in **[P3]**, where SLAO and STO substrates were used. However, in **[P1]** the differences between the films on STO and LSAT remained slightly vague.

The effects of laser fluence and deposition temperature were investigated in **[P2]**. The intrest was to improve the film surface structure for the upcoming magnetic force microscopy measurements, but the effects on the magnetic properties were also studied. The results do not indicate any simple correlation between the laser fluence and the magnetic properties. The M_{sat} values range from 1.39 μ_B/f.u. to 2.43 μ_B/f.u.. Inaccuracy in the films with the low M_{sat} arises from the impurity defect phase, detected with XRD. The non-magnetic $SrMoO_4$ phase diminishes the real value to the apparent M_{sat} value of SFMO phase. Although the films were fabricated with the same pulse number, the different laser fluence between films could also influence the film thickness and therefore cause an error in the M_{sat}. Thickness was measured for one additional

film with smaller pulse number, using x-ray reflectivity analysis. Due to the effects like surface roughness, the x-ray reflectivity interference pattern will die out in thicker films, if the surface roughness is too high. The T_C values range, with different laser fluence values, from 322 K to 348 K and the samples with the higher T_C showed the lower M_{sat}, which could be explained with the higher concentration of oxygen vacancies. Although the T_C is in principle unaffected by the errors in the thin film volume due to impurities, which falsify the M_{sat} results, the impurities might have an effect on magnetic interaction in SFMO phase. The decrease of deposition temperature from 1050 °C to 900 °C showed an increase in T_C from 322 K to 363 K and a decrease in M_{sat} from 2.36 μ_B/f.u. to 1.41 μ_B/f.u. in the phase pure SFMO films. This again could be related to the formation of the lattice site defects in SFMO phase, especially oxygen vacancies or anti-site defects.

The ambient gas atmosphere during the PLD fabrication was, in most cases, Ar gas in approximately 9 Pa pressure. Ar+$H_2$5% mixture was also used when studying the effects of the gas flow and the nature of the gas on the SFMO films **[P5]**. A higher gas flow rate was achieved by utilizing lower background pressure while maintaining the deposition pressure **[P5]**. The higher flow rate with both gas substances, resulted in structural defects evidenced by stronger domain pinning. The higher flow also resulted in an increase in the T_C from approximately 307 K to 325 K and a decrease in the M_{sat} from 2.35 μ_B/f.u. to approximately 1.64 μ_B/f.u.. The nature of the gas between Ar and Ar+$H_2$5% mixture had apparently only little effect on the magnetic properties.

Most of the research on the SFMO films has been about the adjustment of the PLD film fabrication parameters. The effects of *ex-situ* annealing in ultra high vacuum on the SFMO films were also checked in order to obtain higher film quality **[P6]**. The *ex-situ* annealing was conducted for a set of identical SFMO films. The annealing at the highest temperature (550 °C) in the set, resulted in the most significant changes in the magnetic properties. The changes included a surge of the T_C from 314 K to 351 K and a decrease of the M_{sat} from 2.29 μ_B/f.u. to 1.92 μ_B/f.u.. The influence of the annealing in the other SFMO films of the set showed a gradual increase in the T_C towards the results obtained for the sample annealed at the highest temperature. The decrease of the M_{sat} was not witnessed in the other films.

As a conclusion of the investigation of the magnetic properties of SFMO films, one can say that for the optimal performance, SFMO films must exceed thickness of approximately from 100 nm to 150 nm to overcome the substrate induced defects. This of course would not remove the defects, but their effect becomes negligible compared

with the over all results. The properties obtained with a high deposition temperature at 1050 °C can be enhanced by adjusting the PLD ablation temperature to 900 °C, resulting in the increased T_C. However, this might not yet be the optimal deposition temperature, even regarding the magnetic properties, since no thorough optimization for the magnetic properties was conducted. The PLD setup has also gone through alterations, which could influence the deposition, although the fabrication has namely been conducted in similar conditions. The *ex-situ* annealing conducted in high vacuum can also be used to increase the T_C. The most notable increase in the T_C was also accompanied with a decrease in M_{sat}. Based on the current understanding on the influence of lattice site disorder and vacancies, these results would indicate an increase in the oxygen vacancy concentration and a decrease in the ASD concentration, in the results where an increase in T_C was accompanied by a decrease in M_{sat}. However, the sole role of a single type defect is likely insufficient to explain the results. Instead, lattice site vacancies are most likely not limited to oxygen, but grain boundary effects also likely arise, since structural characterization suggests that the films, with possibly higher oxygen vacancy concentrations, also appear to have larger or more low-angle grain boundary defects. Considering the results for T_C and M_{sat} obtained here, similar values can be found from the literature [10, 51, 52, 58]. However, all the results here fall short from the theoretically expected values for both the T_C and the M_{sat}.

4.1.3 Magnetic anisotropy

Magnetic anisotropy is not the main focus of this thesis, but a relevant subtopic of the work and a refinement to a previous investigation [10]. The bulk magnetometry measurements for the most of the thin film samples, included in this work, were measured with the magnetic field, H, parallel with the thin film plane. This is a valid easy-axis hysteresis measurement when the magnetization easy-axis lies within the film plane. In **[P3]**, a shift between in-plane and perpendicular magnetic anisotropy induced by the substrate was reported in SFMO thin films. The SFMO thin films were fabricated on $SrTiO_3$ (STO-1 and STO-2) and $SrLaAlO_4$ (SLAO-1 and SLAO-2) single crystal substrates, with different thicknesses of approximately 30 nm and 120 nm. Thicker films were labeled STO-2 and SLAO-2. Thinner films were labeled STO-1 and SLAO-1.

The effect of magnetic anisotropy was realized mostly through hysteresis loops. An example of the magnetic hysteresis measurements is presented in Figure 10. The presented hysteresis results were obtained for STO-2 and SLAO-2. The results in Figure 10 (a) were obtained while the magnetic field parallel with the film plane. The results in Figure 10 (b) were obtained with the magnetic field perpendicular to the film plane. More accurately, the parallel alignment of the film plane and the magnetizing field, puts the field along (110) SFMO lattice vector (a) and perpendicular alignment along (001) SFMO lattice vector (b). The parallel configuration is a reasonable starting point to conduct magnetic hysteresis measurements. This is because of the demagnetizing effect arising from the sample geometry. Once the sample is magnetized along the easy-axis, this should result in higher magnetization in lower magnetic field, higher remanence magnetization and larger B_c when compared to a measurement where the magnetizing field is along the hard-axis. These attributes would then suggest that SLAO-2, with over-relaxed lattice and with stronger in-plane lattice distortion, has a different magnetization easy-axis from STO-2. In SLAO-2, the magnetization easy-axis is closer to (001) SFMO lattice vector, which is parallel with the normal vector of the film plane, and in STO-2 easy-axis would seem to be closer to SFMO film in-plane vector (110).

The role of magnetic anisotropy in thin films, where ideal crystal structure is altered, can become a crucial variable, since distortion may alter the easy-axis alignment. In **[P3]**, the structural analysis showed a possible over-relaxation in SLAO-1 and SLAO-2 and a clear contribution from low-angle grain boundaries. The over-relaxation is seen as tensile in-plane strain, despite the compressive lattice mismatch between the ideal SFMO and the substrate lattice parameters. With the idea that the over-relaxation of the a and b parameters is countered with the smaller c lattice parameter, the over-relaxation

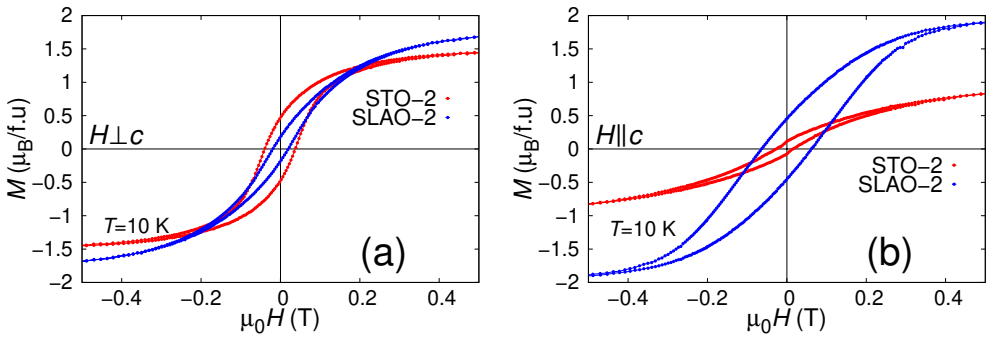

Figure 10. (a) Hysteresis loops for STO-2 and SLAO-2 measured with magnetic field parallel with SFMO (110) lattice vector. (b) Hysteresis loops for STO-2 and SLAO-2 measured with magnetic field parallel with SFMO (001) lattice vector **[P3]**.

is also seen in the lattice size along c axis. This is in the case of positive Poisson's ratio. Indeed tensile strain, along a/b axis, and more significant compressive strain, in ε_c, were observed in SLAO-1 and SLAO-2 films. Due to small tensile strain values, lattice distortion, other defects such as low-angle grain boundaries, were also addressed as a possible source of the shift in anisotropy. However, higher compressive strain in the lattice along c axis provides support for the strain induced perpendicular magnetic anisotropy.

The common stripe or bubble domain pattern is attributed to the perpendicular magnetic aniostropy in thin films. The stripe domain pattern was seen with MFM measurements in SLAO-2 depicting the perpendicular magnetic anisotropy. However, as a more surface sensitive technique and due to the surface effects on the magnetic anisotropy, MFM alone might be unreliable to conclude about the bulk properties in the anisotropy. The MFM results are introduced in section 4.2.3.

4.2 Surface analysis

The giant magnetoresistive components are essentially layer structures, with two or more ferromagnetic layers separated with a spacer layer. For a well-defined layer structure, the initial layer surface, used as a deposition basis for other layers, plays an important role. For a tunneling junction the spacer layer is deemed to be in a nanometer scale. The fine structure may therefore require an atomic scale film growth or at least a result with almost single atomic or unit cell structural deviation. In the absence of a proper layer structure to operate as a valve structure, one ferromagnetic layer can be exposed to, inclusions from other ferromagnetic material acting as pin-holes, Néel coupling between the two ferromagnets or defects and impurities in the transport layer.

4.2.1 Atomic force microscopy

In order to learn about the surface structure of SFMO films, atomic force microscopy measurements were carried out for several films. In part, the purpose was to learn how SFMO film roughness appears in the surface structure and improve upon it, if possible.

Figure 11 shows an example of the AFM results, obtained in **[P3]** for $5\,\mu\text{m}\times5\,\mu\text{m}$ area scans using tapping mode. SFMO films were grown on $SrTiO_3$ and $SrLaAlO_4$ single crystal substrates with thickness corresponding to approximately 30 nm (STO-1 and SLAO-1) and 120 nm (STO-2 and SLAO-2). The AFM measurements were conducted with $5\,\mu\text{m}\times5\,\mu\text{m}$, $10\,\mu\text{m}\times10\,\mu\text{m}$ and $20\,\mu\text{m}\times20\,\mu\text{m}$ scan sizes. The root mean square roughnesses of the films are between 1.9 nm and 5.7 nm and were obtained as an average from all the scans. The smallest roughness values were obtained for STO-1 film. These values are close to the best values obtained in **[P2]** with AFM, where the surface structure of SFMO films was improved by adjusting deposition parameters with lower deposition temperature and/or lower ablation energy density. An improvement towards the lower surface roughness was obtained with a lower deposition temperature, when the deposition temperature was decreased from 1050 °C to 900 °C. The films were all grown on STO substrates with the same pulse number. The obtained improvement in the surface was the decrease of rms roughness from roughly 27 nm to 5 nm. It would seem that the deposition temperature was a more important parameter, in order to obtain an improvement in the surface roughness. The films used in **[P3]** were fabricated with the parameters of the improved surface structure in **[P2]**. This apparently provided more stability in the included magnetic force microscopy measurements, since at low lift heights the tip easily crashed with the sample surface. The surface of the thinner films (STO-1 and SLAO-1) have terrace like structures on top of a smooth background

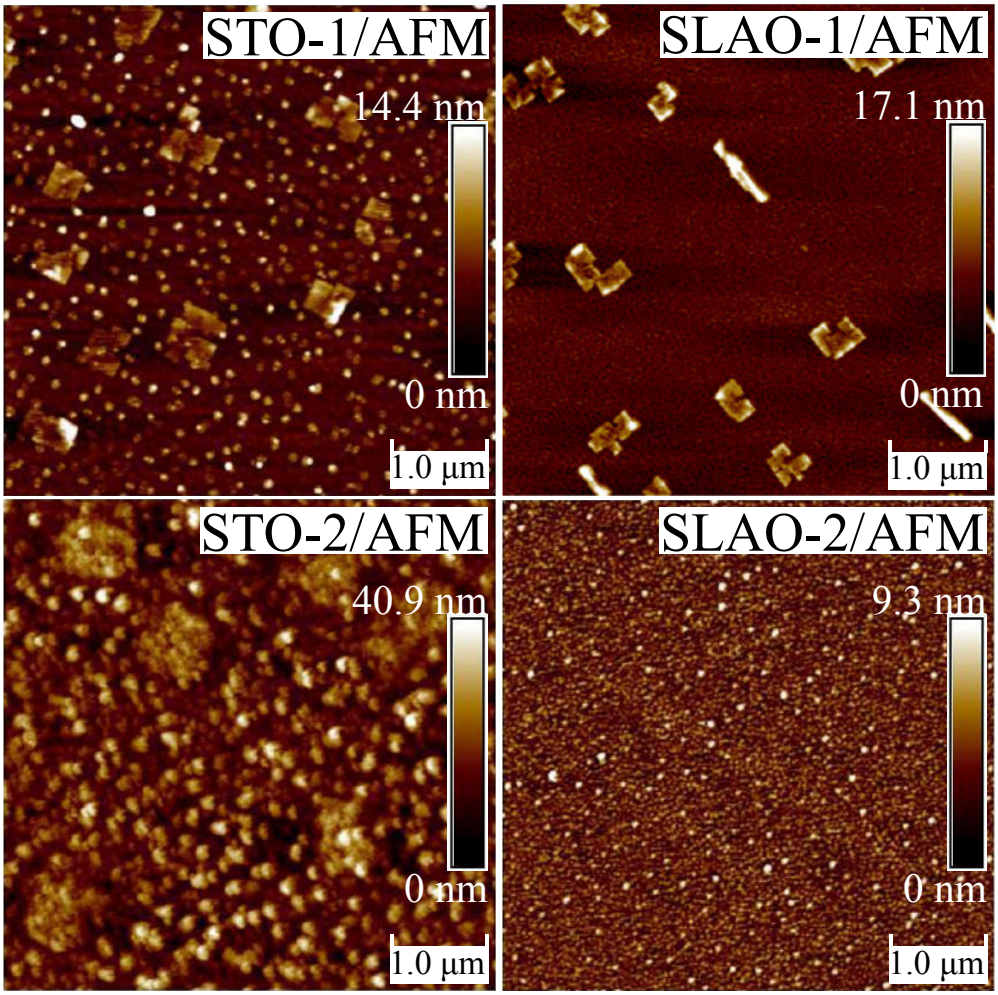

Figure 11. 5×5 μm^2 size AFM images for SFMO films fabricated on STO and SLAO substrates **[P3]**.

surface. These structures are apparently absent from the surface of the thicker films. Similar structures and surface roughness values have been observed earlier [67]. The terrace like structures have been associated with the film growth, when exhibiting a single unit cell sized step between terraces [67, 69]. The terraces here, exceed the size of a single or a single half of SFMO unit cell, but the structure edges have a well-defined perpendicular orientation amongst one another. This type of orientation of structures could be related to the epitaxial growth of the thin film [57, 70].

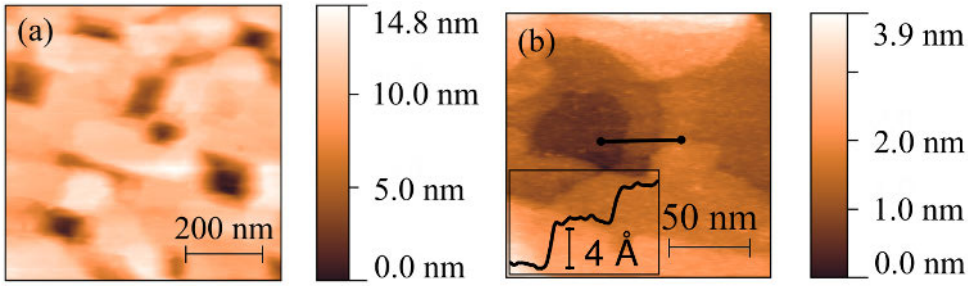

Figure 12. STM images for SFMO film. (b) is a zoom-in of (a) **[P4]**.

4.2.2 Scanning tunneling microscopy

PLD deposited samples do show a single unit cell layer-by-layer growth mode in several films, SFMO and others [69, 71]. However, obviously the single layer growth does not always appear as a result of PLD fabrication [19, 55, 57, 67, 72]. In two investigations included in this work **[P2]** and **[P3]**, no clear evidence of a single SFMO unit cell layer growth was observed. A more accurate investigation of the surface structure did show layers with height approximately equal to 4 Å, one half of the SFMO double perovskite *c* parameter **[P4]**. This investigation was conducted with low temperature scanning tunneling microscopy operating at 84 K temperature and films surface height deviation, from a larger area, greatly exceeded the single unit cell size. Considering the fabrication of conventional multilayer structures as spin valves, the surface structure sets an unfortunate obstacle. A nanometer thick interface layer of couple of square micrometers in area would unlikely produce a well-defined separation between the two spin-polarized ferromagnets, unless the junction area is significantly reduced.

An example of the results obtained for the SFMO film, deposited with 500 pulses, is presented in Figures 12 (a) and (b). The surface of the SFMO film presented in Figure 12 (a) consists of holes, penetrating roughly 10 nm from the top SFMO layers towards the substrate. This would be approximately half of the thickness of the film. The appearance of the hole structure possibly results from the film growth including an island-like growth mode. The multiple growth sites due to the island growth involve a unit cell layer-by-layer growth as is indicated in Figure 12 (b). The film growth during the deposition involves the combination of island and layer growths resulting in an empty area between growth sites. Eventually, this space becomes reduced, resulting in holes in the film structure. The hole structure does not appear similarly in a thicker SFMO film.

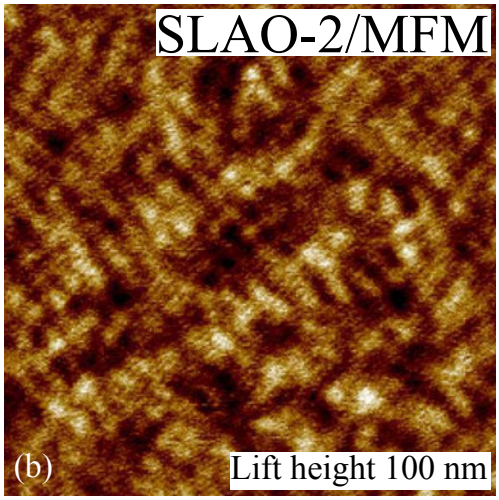

Figure 13. MFM image for SFMO film fabricated on SLAO substrate **[P3]**.

However, the height variation is roughly the same between the thicker and the thinner film.

4.2.3 Magnetic force microscopy

The used AFM setup utilizes the characterization of long range magnetic forces at room temperature. The interactions between the magnetic sample and the magnetic tip allow the reconstruction of the sample surface domain structure. The MFM measurements were performed on SFMO samples deposited on STO and SLAO substrates. The samples are the same as the ones used in the magnetic anisotropy study **[P3]**.

An accurate quantitative analysis of the MFM results is difficult, since the magnetization of the measuring tip can be influenced by the magnetic sample. Therefore, the obtained results become slightly more qualitative in nature. In addition, the long range forces include not only the magnetic, but also the electrostatic forces. An example of the MFM result is presented in Figure 13. This is a result obtained from SLAO-2 sample with 100 nm lift height. The sample film exhibited perpendicular magnetic anisotropy according to the magnetization hysteresis measurements. Traces of stripe patterns in the surface domain structure provide an additional support for the argument of perpendicular anisotropy. However, as a surface sensitive technique, the MFM results alone should not be considered conclusive regarding the overall analysis of the magnetic anisotropy.

To compare the MFM results for different samples, a radial profile of the Fourier

transform was taken from the MFM images. Structures seen in the MFM results provided a distribution depicting smaller magnetic structures in SLAO-2 (thick SFMO film on SLAO) compared with STO-2 (thick SFMO film on STO). This was also the apparent impression. It was suggested that the observed smaller magnetic structures, combined with larger structural defects, could play their part in stronger domain pinning **[P3]**. SLAO-2 showed evidences of more profound structural defects both in the structural and magnetic characterization.

4.2.4 Electronic surface structure

Due to the immediate role in the magnetic properties, the electronic analysis of SFMO has been historically focused mainly on Mo and Fe states. Spectroscopy techniques have been used to provide evidence about the highly mixed degenerate valence states between Fe^{3+}-Mo^{5+} and Fe^{2+}-Mo^{6+} in the ferrimagnetic orientation [24, 25]. The elemental detection capability makes x-ray photoelectron spectroscopy (XPS) the particular focus of interest for example in additional phase purity investigation. When XRD relies on the structural ordering and related diffraction from the crystal structure, XPS provides a surface sensitive impurity analysis relying on elemental specific binding energy states. As a part of the surface analysis of SFMO thin films, a set of identically deposited SFMO samples were investigated with XPS, before and after *ex-situ* annealing **[P6]**. The annealing was conducted in an ultra high vacuum chamber connected directly to the XPS setup. The target temperature for the annealing for one sample was 200 °C (473 K), 400 °C (673 K) or 550 °C (823 K), while one of the samples was only stored in the XPS chamber. The annealing temperature was reached by increasing the temperature by 10 °C per minute. The annealing temperature was maintained for an hour, after which the temperature was decreased back to the ambient temperature at the same rate.

The results for the survey spectrum, before and after the annealing, are presented for the sample annealed at the highest temperature in Figure 14. The details are identified and labeled with the elemental states with the corresponding binding energies in Table 5. The most notable features indeed arise from the well-expected Sr_2FeMoO_6 elemental states, along with unavoidable carbon contamination. Carbon contamination is present, due to the sample exposure to the ambient room atmosphere before the measurement.

The detailed high resolution XPS spectra were obtained for Mo 3d, Sr 3d and O 1s. The electronic states were identified with pseudo-Voigt profiles. Fitting was performed using the SPANCF curve fitting macro package, as presented in [73, 74] using Igor Pro fitting program, after subtracting the Shirley type background. The carbon states were also recorded in more detail, but no identification of the single electronic states was done. In the sample, which was only stored in the ultra high vacuum chamber without a heat treatment, the carbon states remain essentially unaffected between the XPS measurements. However, the annealing performed at the highest temperature of 550 °C clearly resulted in diminished carbon contamination, the effect being less apparent in the samples annealed at lower temperatures. This was evidenced by a decrease in the relative peak intensities between carbon and Mo 3d, Sr 3d, O 1s states. The results for the detailed XPS analysis for Mo 3d, Sr 3d and O 1s are presented in Figures 15 (a)-(c)

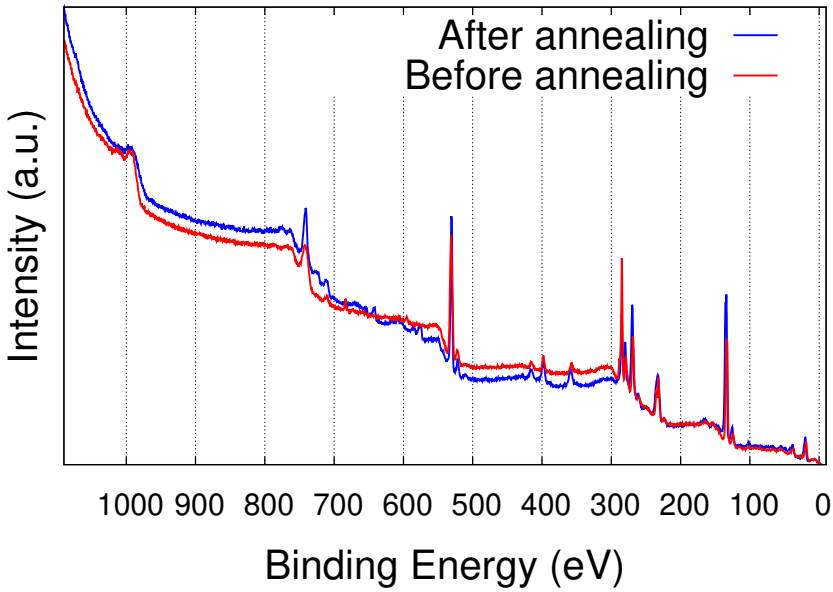

Figure 14. The full XPS survey between 1100 eV and 0 eV obtained for SFMO film before and after the temperature annealing at 550 °C **[P6]**.

Table 5. The B.E. values for the most notable features seen in XPS survey **[P6]**.

B.E. (eV)	Elemental state	B.E. (eV)	Elemental state
21	O 2s	358	Sr 3s
37	Mo 4p	398	Mo $3p_{3/2}$
135	Sr 3d	415	Mo $3p_{1/2}$
232	Mo 3d	530	O 1s
269	Sr $3p_{3/2}$	710	Fe 2p
280	Sr $3p_{1/2}$	740	O (Auger KVV)
285	C 1s		

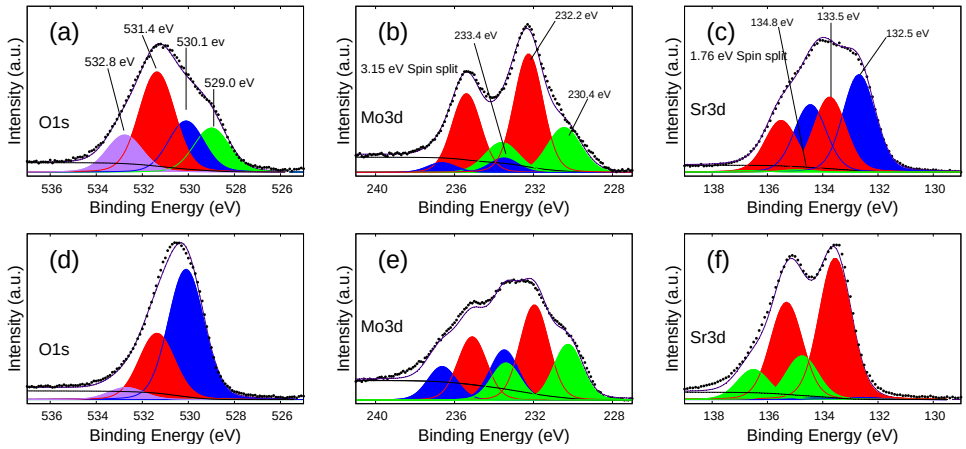

Figure 15. The detailed photoelectron spectra for O 1s, Mo 3d and Sr 3d both before ((a), (b) and (c)) and after ((d), (e) and (f)) the annealing. The identified states in Mo 3d contribute to $Mo^{\gamma+}$-(green), Mo^{5+}-(red) and Mo^{6+}-states (blue) **[P6]**.

before and (d)-(f) after the annealing. The results are for the sample annealed at the highest temperature of 550 °C.

The results for O 1s electronic states for the preliminary (a) and the annealed (d) SFMO film are discussed. Due to the complex photoelectron spectra, the accurate identification of the oxidation states and their origin is rather difficult. As a part of the contamination removal, the demise of O 1s states after the annealing may well be resulted by the removal of the hydroxyl and the carbonate groups, outside the perovskite structure of SFMO. The removal of the possible hydroxyl and carbonate traces becomes more apparent once the annealing is conducted at higher temperature, while the sample stored in the vacuum, without actual annealing, is practically unaffected.

The molybdenum 3d spectrum results in Figure 15 (b) and (e) are adequately explained with three spin-orbit splitted peak pairs, with binding energy around 233 eV. The spin-orbit splitting in the oxidation state, between binding energy values, was approximately 3.2 eV. The oxidation states were identified as $Mo^{\gamma+}$ (green), Mo^{5+} (red) and Mo^{6+} (blue), where $\gamma \leqslant 4$ and lower binding energy corresponding to the lower oxidation state. The results before the annealing are dominated by Mo^{5+} states, with less contribution from $Mo^{\gamma+}$ and only a minor signal arising from Mo^{6+}. Compared to the $Mo^{\gamma+}$ and Mo^{6+} states, the Mo^{5+} becomes less representative in the spectrum after the annealing and the spectrum is changed towards a more mixed valence in Mo 3d. As it has already been demonstrated with Mo 3d photoemission spectra, the annealing would

seem to alter the electronic state of SFMO perovskite. The same is evident in Sr 3d spectra presented in Figures 15 (c) and (f), respectively before and after the annealing. Sr 3d binding energy spectra, close to 135 eV, is depicted by three spin-orbit splitted peak pairs, with approximately 1.8 eV spin-orbit splitting in binding energy. The results, obtained before and after the annealing, differ from each other in the sense that from the three oxidation states the low binding energy state is absent from the results obtained after the annealing and the high binding energy state is absent from the results before the annealing. This could either suggest a significant Fermi level shift or derivation and demise of an oxidation state. From the results obtained for the sample annealed at 400 °C, all three oxidation states can be identified with more clarity.

Since the laboratory setup XPS provides information primarily from surface elements, the identification of Mo 3d and Sr 3d oxidation states was supported with the complementary hard x-ray photoelectron spectroscopy (HAXPES) results. The HAXPES measurements were carried out at HIKE end-station of the KMC-1 beamline in BESSY II. The sample was SFMO thin film fabricated at 950 °C on Nb doped $SrTiO_3$ single crystal substrate. With higher excitation energies of 2020 eV and 5000 eV, a larger detection depth is obtained, when compared to the laboratory setup XPS and the results obtained provide information deeper inside the thin film bulk. The HAXPES results for O 1s, Mo 3d and Sr 3d appeared similar to the results obtained after the annealing with laboratory setup XPS, particularly for the film annealed at the highest temperature. This suggests that the results obtained with the conventional laboratory setup XPS are relevant to the electronic structure of SFMO and do not simply arise from the immediate surface contamination.

The involvement of the XPS analysis in this work was to study the effects of *ex situ* annealing on SFMO thin films. As a surface sensitive technique, some of the possible disadvantages arising in the multilayered spin valve structures from SFMO surfaces can be addressed. The XPS analysis confirms that to some extent, SFMO films are contaminated at the surface by the phases outside of SFMO perovskite due to the exposure to ambient atmosphere. The annealing provides an effective cleansing from the organic impurities. This is depicted by the demise of C 1s signal, and most likely by the contraction of the high energy oxygen components, compared with SFMO elements. The tendency towards a more mixed valence after the annealing in the Mo 3d spectra could be related to the impurity removal, but SFMO has also being shown to exhibit intrinsic mixed valence between Mo $3d^{5+}$ and Mo $3d^{6+}$ [24, 25]. The HAXPES measurements support this idea and hence the results obtained after the annealing appear as they do,

most likely due to the mixed valence in SFMO. The ferrimagnetic ordering has been shown to exhibit degenerate valence states between Fe^{2+}-Mo^{6+} and Fe^{3+}-Mo^{5+} states. A conclusive data for Fe^{2+}/Fe^{3+} states was not obtained with the laboratory XPS setup. The results were obtained with the HAXPES and the mixed valence between Fe^{2+} and Fe^{3+} was identified. The contribution from Fe states can be recognized from the laboratory survey spectrum. However, the resolution of this survey is not sufficient for an adequate identification of fine details in the valence. In addition, a considerable background signal makes the identification even more difficult. In the photoelectron spectra for Sr 3d, the state at 133.5 eV was contributed to $3d_{5/3}$ Sr^{2+} in the perovskite structure. This decision was to some extent in contradiction with previous publications and indeed leaves room for a debate. However, the conclusion was also supported by additional reports and the HAXPES measurements. This identification leaves an unidentified photoelectron state at low binding energy. The absence of this state, in the results obtained after the annealing, could be related to the removal of the contaminant surface phases.

5 Sr_2FeMoO_6 spin valve prototype

The results presented in this thesis confirm that the fabrication of a well-defined multilayer structure, with a junction area of several micrometers, is inconvenient with a regular metal transport layer or with an insulator layer. This is evident from the structural surface characterization, where the surface roughness is far from what would be expected for a single unit cell layer growth. Therefore, the approach for spin valve devices taken here is to utilize organic semiconductor as a transport layer. This offers flexibility to the device structure, since multiple reports have shown that devices with over 100 nm thick transport layer can be used to obtain the appropriate magnetoresistive response [75]. Here, the results related to the spin valve fabrication, supportive magnetometry and magneto-transport measurements and spin valve effect in SFMO based spin valve devices are described **[P7]**.

For the spin valve fabrication, SFMO film was deposited with the PLD with 2000 laser pulses at 900 °C on STO single crystal substrate. After the film deposition, the film was etched with ultraviolet photolithography using positive photoresist with a plastic shadow mask and nitric acid solution. The etching resulted in the single SFMO sample consisting of one approximately 100 μm wide stripe and two approximately 200 μm wide stripes. Patterned SFMO film was then cleaned with isopropanol. In part due to the results obtained in the work, the available options for the multilayer deposition and already proven functionality in organic semiconductor based spin valve devices [75], organic tris-(8-hydroxyquinoline)aluminum (Alq_3) was chosen as a material for the interphase layer. Alq_3 layer, ferromagnetic cobalt and protective aluminum layers were vacuum evaporated on top of SFMO stripes, in the mentioned order using a thermal evaporator. The deposition resulted in approximately 45 nm, 16 nm and 2 nm thick Alq_3, Co and Al layers, respectively. The deposition pressure in the evaporator chamber was kept between 5 mbar and 10 mbar.

An identical patterned SFMO thin film, without the following layers, was used in the supportive magnetometry measurements. The results for ZFC/FC magnetizations in 100 mT are presented in Figure 16 (a), where a regular magnetization decay with increasing temperature is seen. The results are normalized according to FC magnetization at 10 K. The inset presents the first order magnetization derivative as a function of temperature, demonstrating T_C around 325 K. The normalized magnetization hysteresis measurement results are presented in Figure 16 (b) for the same SFMO film, in addition to the results for Co film deposited on a glass plate. While the results for SFMO are well within the line of the other presented results for SFMO films, with approxi-

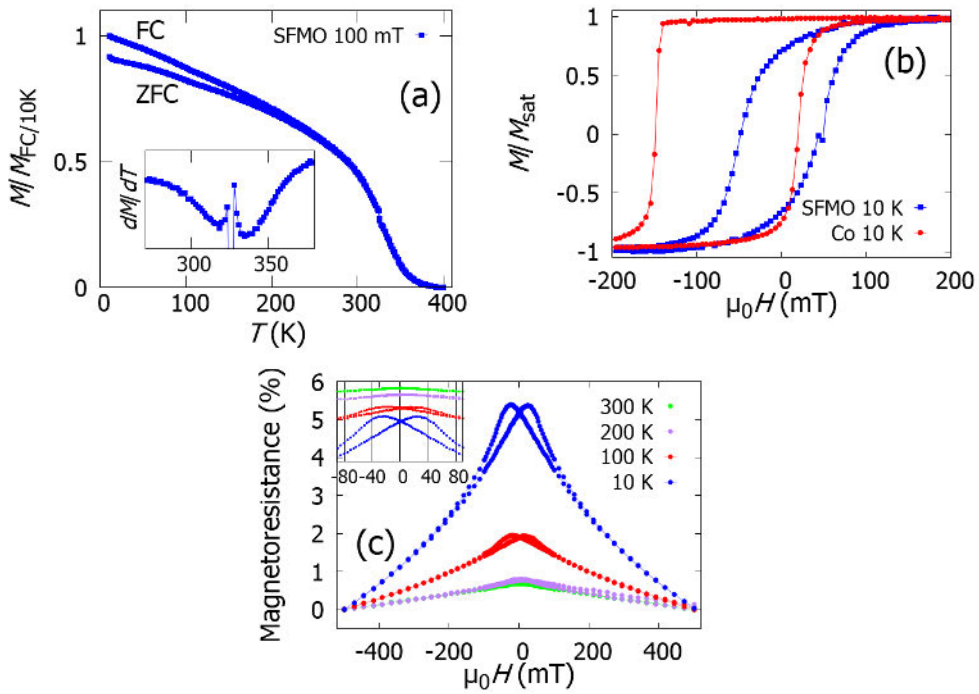

Figure 16. (a) ZFC/FC-magnetizations of the patterned SFMO thin film. (b) Hysteresis loops for the patterned SFMO thin film and Co film on a glass plate. (c) Magnetoresistance of the 100 μm wide SFMO stripe used in the spin valve multilayer structure **[P7]**.

mately B_c equal to 46 mT and 0.68% remanence magnetization from the saturation, the hysteresis for Co film showed a large exchange bias. The respective field for zero magnetization showed values around -149 mT and 19 mT. The large exchange bias could be related to Co oxidation and to the coupling between antiferromagnetic CoO and Co metal [80].

Magnetoresistive measurements for SFMO film were measured for 100 μm wide SFMO stripe in the SFMO/Alq_3/Co/Al multilayer device. The results are presented in Figure 16 (c). The applied magnetic field was parallel with the SFMO plane along the (110) lattice vector. Magnetoresistance was calculated according to $MR = (R_H - R_{500mT})/R_{500mT}$, were R_H is the resistance in magnetic field H and R_{500mT} is the resistance in 500 mT magnetic field. The magnetoresistance response of the SFMO stripe at 10 K temperature is roughly 4.9%. The resistance is smaller at higher fields and shows a clear hysteretic low field magnetoresistance response. The hysteretic resistance with the magnetic field is characteristic for a system, where the charge carrier transport includes tunneling between spin polarized magnetic grains. The magnetic field orients the magnetic moments pointing to a same direction reducing the spin dependent scattering, which again decreases the resistance. The hysteresis in the magnetoresistance rises due to the magnetic hysteresis related to the domain pinning. The results in Figure 16 (c) show that the magnetoresistance decreases significantly at higher temperatures, already at 100 K, and the low field response is practically absent at 200 K and higher temperatures. This suggests that the spin dependent scattering of charge carriers is more significant at low temperatures. Since basically all the work, included in this thesis, confirms the fabrication of high quality SFMO films with epitaxial growth, the origin of the magnetoresistance is most likely not due to grain defects, like in polycrystalline samples. Instead, subtle structural defects like low-angle grain boundaries and antiphase boundaries may contribute to the results [51].

A part of the key magnetotransport results obtained for SFMO/Alq_3/Co/Al multilayer structures is presented in Figure 17. The results represent the magnetoresistive response at 10 K for a junction with (a) 200 μm wide SFMO stripe and (b) 100 μm wide SFMO stripe. The results show hysteretic resistance maxima with respect of the magnetic field, which is characteristic for a working spin valve device. Approximately 20% and 30% magnetoresistance, respectively for (a) and (b), was measured at 10 K. These values compare well with the few previously published results that exist for SFMO based tunnel junctions, where 10%-50% magnetoresistance responses have been obtained by others [76, 77]. The junctions here showed a notable decrease in the

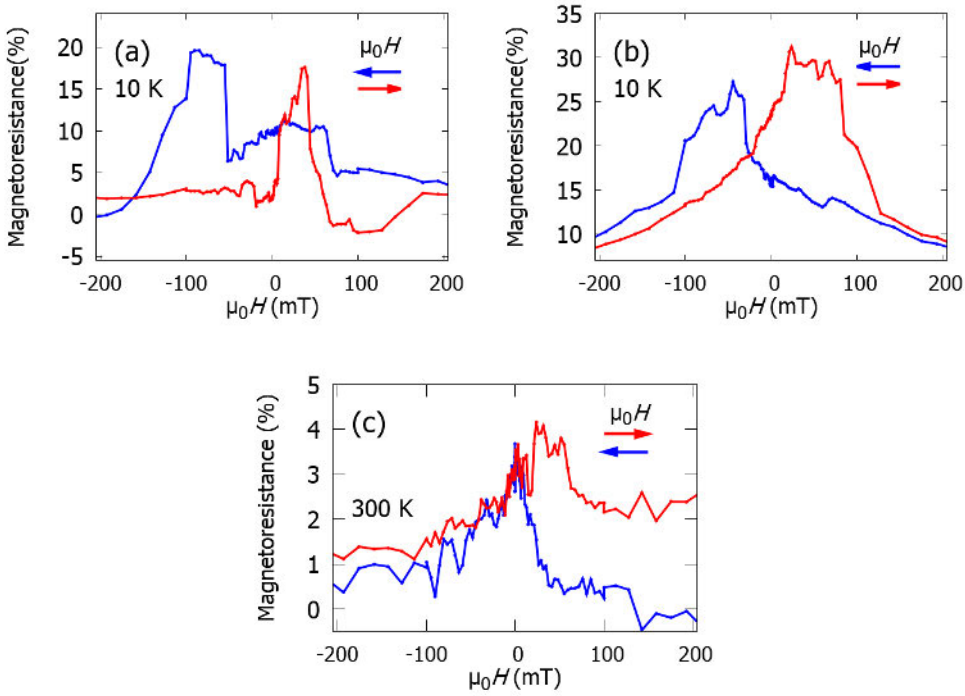

Figure 17. Magnetoresistance signal from the two SFMO/Alq_3/Co/Al junctions at 10 K, a) with 200 μm wide SFMO stripe, b) with 100 μm wide SFMO stripe. Magnetoresistance obtained from the junction with 200 μm wide SFMO stripe at 300 K **[P7]**.

magnetoresistive response at higher temperatures, while also losing the hysteretic nature of the resistive switching with magnetic field. The loss of the spin valve effect with increasing temperature could be related to the demise of spin polarization in ferrimagnetic SFMO or at least to the demise of the spin polarization at the SFMO/Alq_3 interface, as it has been reported for $La_{1-x}Sr_xMnO_3$ (LSMO) based devices [78]. The decrease in the magnetoresistance seen for SFMO in Figure 16 (c) would apparently support this claim on the loss of the spin polarization in SFMO. However, the spin memory can be lost during the charge transportation through Alq_3 and a decrease in spin relaxation length with increasing temperature may have a part in the decrease of the magnetoresistance response [79].

Although the magnetoresistance response showed a clear decrease with increasing temperature, it must be noted that approximately from 2% to 4% magnetoresistance was observed at 300 K in the junction with 200 μm wide SFMO stripe in Figure 17 (c). This

is a considerable magnetoresistance response at room temperature.

The hysteretic resistance maxima correspond to the antiparallel alignment of the magnetic moments in the ferri- and ferromagnetic SFMO and Co layers. In a separate Co sample on a glass plate, an exchange bias was detected in the magnetization hysteresis measurements. An exchange bias, due to Co oxidation [80], could be affecting the magnetic switching in the multilayer structure, which could explain the asymmetry in the magnetic field corresponding to the resistance maxima. Multiple research projects declare a negative magnetoresistance in organic semiconductor spin valve devices [78, 79, 81–84]. This means that the antiparallel alignment of the magnetic moments between the ferromagnetic layers results in a decrease of resistance. The negative magnetoresistance has historically been first explained through negative spin-polarization in the ferromagnetic Co layer [79], which causes the expected positive magnetoresistance sign to reverse. The positive magnetoresistance, reported here and the difference with the previous research, could be related to an ill defined Alq_3 transport layer. However, the difference could also be explained by the fact that according to the band structure calculation, SFMO itself should be expected to be negatively spin polarized [1, 85]. Assuming the negative spin-polarization in the ferromagnetic Co layer, as reported in the other organic semiconductor based spin valve devices, the device here would be expected to result in the positive magnetoresistance response. These remarks are within the line of previously published results for SFMO/STO/Co and LSMO/STO/Co tunneling junctions [86, 87], in which the magnetoresistance sign is argued to reverse between different junctions, because of the inverse spin-polarization between LSMO and SFMO layers. This scenario addresses the phenomenon of inversed magnetoresistance in simple terms. The conductance through a junction is proportional to the density of states at the Fermi level. When the spin polarization at the Fermi level between two ferromagnetic layers is the same (positive or negative), an increase in resistance, with antiparallel orientation of the magnetic moments, is to be expected. Once the polarization between the two layers is mixed, the antiparallel alignment of magnetic moments results with the low resistance state.

The results presented here demonstrate, to our knowledge, the first results for SFMO based organic semiconductor spin valve device and are one of the only reports for SFMO spin valves in general [76, 77]. The early results clearly provide an interesting field of further research. This includes the obvious parameter variations and optimization in the current device design. However, the very physics behind for example the spin relaxation in organic semiconductor remains open and therefore also the demise of the

spin valve effect at higher temperatures is not completely clear. There are also questions about the stability of the obtained spin valve prototype. Although these remarks are rather speculative in nature, it would seem that the spin valve prototype does deteriorate over time. Immediately after the deposition, the prototype exhibits magnetoresistive attributes, which are evidenced by repeatable measurement results. When becoming more exposed to ambient atmosphere and more measurements or when the devices are stored for a prolonged period of time, the desired attributes seem to vanish. This could perhaps be due to instability of the organic transport layer. This discussion about the stability of the SFMO spin valve prototype demonstrates only early observations.

6 Conclusions

This thesis considers the SFMO thin film analysis, separating bulk and surface analysis, and the fabrication of SFMO based spin valve prototype. The goal has been in part to provide a picture on the effects of PLD growth process to the film properties. The handled parameters in the fabrication process included film thickness, laser fluence, temperature, substrate material, gas flow rate and the nature of the ambient gas during the deposition. It was realized that the film thickness must exceed roughly 100 nm in order to the substrate induced defects become insignificant, regarding Curie temperature (T_C), saturation magnetization (M_{sat}) and domain pinning. The films with small thickness exhibited lower T_C, lower saturation magnetization and stronger domain pinning. Increasing film thickness resulted in an improvement, or putting more neutral with a change, in these attributes until the saturation of the attributes with films over 100 nm thickness. This sets a possible threshold value for the film thickness to achieve the ideal film properties.

The laser fluence could be crucial for the phase purity of SFMO films. In the case where laser fluence was altered, two out of the four samples showed a clear signal from $SrMoO_4$ impurity phase. Lower deposition temperature from 1050 °C to 900 °C resulted in higher T_C while maintaining phase purity. The lower deposition temperature seemed to push the T_C of the thinner films above what was obtained for SFMO thickness series, where the deposition was performed at higher temperatures. On STO substrate thicker SFMO film still had higher T_C. However, on SLAO there was no difference in the T_C between thinner and thicker SFMO film, but the effect of substrate induced defects seemed larger regarding for example the saturation magnetization, coercive field and XRD peak broadening.

The substrate was also seen to influence the magnetic anisotropy in the SFMO films. The difference in magnetization easy axis was recognized between the films fabricated on STO and SLAO substrates. The phenomenon could be due to lattice site defects like compressive versus tensile strain or low angle grain boundaries.

The influence of the nature and the flow rate of the gas was analyzed and it was concluded that higher flow rate of the gas resulted in more structural defects. This was analyzed with x-ray diffraction. The broadening in x-ray diffraction peaks results to some extent from structural deviation in the characterized samples. Regarding the magnetic analysis, the higher flow rate of the gas seemed to result in SFMO phase with more oxygen vacancies. This is suggested by the higher T_C and lower saturation magnetization. However, no direct evidence from oxygen vacancy states were obtained.

The nature of the gas, between Ar and Ar+$H_2$5%, did not seem to have a crucial role in terms of film properties.

The surface analysis was included as a crucial part of this work. Since atomically flat interface region is favorable in multilayered nanostructures, the surface study is included in the initial characterization and as a mid-term goal before the ultimate goal of constructing SFMO based spin valves. The surface analysis in this work included improving the surface roughness, which was observed being well above atomically flat height boundaries. By adjusting the deposition temperature from 1050 °C to 900 °C, the surface roughness was improved from 27 nm to 5 nm. The roughness was evaluated as root-mean-square (rms) roughness. The smallest rms value, below 2.0 nm, was obtained for SFMO film fabricated on STO substrate at 900 °C. While all the films studied here exhibited roughness with height deviation over a single SFMO unit cell, a single or a single half of SFMO unit cell terrace-like structure was also observed. However, the single terrace structure is shaded in large area scans of several micrometers. The results from the surface analysis set an obstacle if planning for TMR devices with junction area of several square micrometers or more.

Magnetic domains were investigated with magnetic force microscopy. Although this analysis does provide additional evidence of perpendicular magnetic anisotropy in the form of bubble stripe domain pattern in the SFMO films deposited on SLAO substrate, as a surface technique MFM alone might be insufficient to draw conclusions considering magnetic bulk properties of the samples. However, the role of anisotropy might become crucial if fabricating multilayered structures, where the two ferromagnetic layers exhibit different magnetization easy-axes. This could influence the switching between relative orientation of magnetizations, thus removing the alteration between antiparallel and parallel alignment.

The electronic structure of SFMO film surface showed clear evidence of additional impurity traces outside SFMO phase. Instead of an inappropriate deposition condition, these impurity traces are due to exposure to ambient environment. Foreign phases outside of SFMO consisted of organic phases. Annealing done *ex-situ* in high vacuum was performed in order to provide a cleansing from surface contamination. Ideally this could result in a refined interface for multilayered systems. Indeed the trace of organic impurity phases was realized through photoemission spectroscopy analysis as a demise of C 1s states. In addition to impurity analysis, photoemission spectras of O 1s, Mo 3d and Sr 3d states were characterized. The unannealed O 1s spectra appeared to be influenced by the additional states outside of SFMO, while these traces were removed after

the annealing. The comparison with HAXPES measurements suggests that the results obtained from the annealed SFMO samples are more related to pure SFMO phase. In addition, the annealing resulted in the surging of T_C from roughly from 310 K to 350 K, without any unwanted trade-offs.

As an important final analysis to this work, fabrication and magneto-transport measurement results were reported for SFMO based organic semiconductor spin valve devices. SFMO junctions with different SFMO stripe widths, showed approximately from 20% to 30% magnetoresistance at 10 K temperature. The demise of the magnetoresistance response at higher temperatures was observed, but a notable magnetoresistance from 2% to 4% was still observed close to room temperature. Both, the demise of the magnetoresistance at higher temperatures and the magnetoresistance sign, were discussed in relation to other research work done by others.

References

[1] K.-I. Kobayashi *et al.*, Nature **395**, 677 (1998).

[2] B. Dieny, J. Magn. and Magn. Mater. **136**, 335 (1994).

[3] P. Grünberg, J. Magn. and Magn. Mater. **226**, 1688 (2001).

[4] R. J. D. Tilley, *Perovskites : Structure-Property Relationships* (John Wiley & Sons, 2016).

[5] M. Borowski, *Perovskites: Structure, Properties and Uses* (Nova Science Publishers, 2010).

[6] S. Nakamura and K. Oikawa, J. Phys. Soc. Jpn. **72**, 3123 (2003).

[7] R. J. D. Tilley, *Defects in Solids* (John Wiley & Sons, 2008).

[8] LI. Balcells *et al.*, Appl. Phys. Lett. **78**, 781 (2001).

[9] D.D. Sarma *et al.*, Solid State Communications **114**, 465 (2000).

[10] M. Saloaro *et al.*, J. Phys. Cond. Mat. **27**, 386001:1 (2015).

[11] D. Stoeffler and S. Colis, J. Phys. Cond. Mat. **17**, 6415 (2005).

[12] D. Stoeffler and S. Colis, Materials Science and Engineering **126**, 133 (2006).

[13] M. Saloaro *et al.*, ACS Appl. Mater. Interfaces **8**, 20440 (2016).

[14] M. Hoffmann *et al.*, J. Phys. Cond. Mat. **30**, 305801 (2018).

[15] H. Deniz *et al.*, J. Mater. Sci. **50**, 3131 (2015).

[16] J. Raittila *et al.*, J. Phys. Chem. Solids **67**, 1712 (2006).

[17] J. Santiso, A. Figueras, and J. Fraxedas, Surf. Interface Anal. **33**, 676 (2002).

[18] N. A. Kalanada *et al.*, Journal of ELECTRONIC MATERIALS **45**, 3466 (2016).

[19] D. Kumar and D. Kaur, Physica B **405**, 3259 (2010).

[20] W. A. Adeagbo *et al.*, Phys. Rev. Mater. **2**, 083604 (2018).

[21] S. Vasala and M. Karppinen, Prog. Solid State Ch. **43**, 1 (2015).

[22] M. Besse *et al.*, Europhys. Lett. **60**, 608 (2002).

[23] O. Erten *et al.*, Phys. Rev. Lett. **107**, 257201 (2011).

[24] J. S. Kang *et al.*, Phys. Rev. B **66**, (2002).

[25] J. H. Kim *et al.*, J. Korean Phys. Soc **43**, 416 (2003).

[26] T. Saha-Dasgupta and D. D. Sarma, Phys. Rev. B **64**, 064408 (2001).

[27] A. S. Ogale, S. B. Ogale, R. Ramesh, and T. Venkatesan, Appl. Phys. Lett. **75**, 537 (1999).

[28] M. García-Hernández, J. L. Martínez, M. J. Martínez-Lope, M. T. Casais, and J. A. Alonso. Phys. Rev. Lett., **86**:2443–2446, 2001

[29] J. Navarro *et al.*, J. Phys. Cond. Mat. **13**, 8481 (2001).

[30] J. Navarro, J. Nogués, J. S. Muñoz, and J. Fontcuberta, Phys. Rev. B **67**, 174416 (2003).

[31] D. Stoeffler and S. Colis, Materials Science and Engineering B **126**, 133 (2006).

[32] A. B. Muñoz-García, M. Pavone, and E. A. Carter, Chemistry of Materials **23**, 4525 (2011).

[33] D. Topwal *et al.*, Phys. Rev. B **73**, 094419 (2006).

[34] B. Aguilar, O. Navarro, and M. Avignon, Europhys. Lett. **88**, 67003 (2009).

[35] B. J. Park *et al.*, J. Magn. and Magn. Mater. **272-276**, 1851 (2004).

[36] H. Wu *et al.*, Solid State Commun. **177**, 57 (2014).

[37] R. Kircheisen and J. Töpfer, Journal of Solid State Chemistry **185**, 76 (2012).

[38] D. Stoeffler and S. Colis, J. Magn. and Magn. Mater. **290-291**, 400 (2005).

[39] T. Fix *et al.*, J. Appl. Phys. **98**, 023712 (2005).

[40] J. M. D. Coey, *Magnetism and magnetic materials* (Cambridge University Press, 2010).

[41] F. Brailsford, *Physical Principles of Magnetism* (D. Van Nostrand Company LTD., 1966).

[42] B. D. Cullity, *Introduction to Magnetic Materials* (Addison-Wesley Publishing Company, Inc., 1972).

[43] M. Getzlaff, *Fundamentals of Magnetism* (Springer, 2008).

[44] G. Binasch, P. Grünberg, F. Saurenbach, and W. Zinn, Phys. Rev. B **39**, 4828 (1989).

[45] M. N. Baibich *et al.*, Phys. Rev. Lett. **61**, 2472 (1988).

[46] R. M. White, *Quantum Theory of Magnetism* (Springer, 2007).

[47] X. Zhang and W. Butler, *Theory of Giant Magnetoresistance and Tunneling Magnetoresistance. In: Xu Y., Awschalom D., Nitta J. (eds) Handbook of Spintronics* (Springer, 2016).

[48] M. B. Salamon and M. Jaime, Rev. Mod. Phys **73**, 583 (2001).

[49] E. Dagotto, *Nanoscale Phase Separation and Colossal Magnetoresistance: The Physics of Manganites and Related Compounds* (Springer-Verlag, Berlin, 2003).

[50] O. N. Meetei *et al.*, Phys. Rev. B **87**, 165104 (2013).

[51] D. Sa̹nchez *et al.*, J. Appl. Phys. **96**, 2737 (2004).

[52] A. Di Trolio *et al.*, J. Appl. Phys. **100**, 013907 (2006).

[53] J. Z. Sun and A. Gupta, Annu. Rev. Mater. Sci. **28**, 45 (1998).

[54] D. B. Chrisey and G. K. Hubler, *Pulsed Laser Deposition of Thin Films* (John Wiley Sons Inc., 1994).

[55] P. Paturi, M. Metsänoja, and H. Huhtinen, Thin Solid Films **519**, 8047 (2011).

[56] T. Suominen, J. Raittila, and P. Paturi, Thin Solid Films **517**, 5793 (2009).

[57] R. P. Borges *et al.*, Thin Solid Films **429**, 5 (2003).

[58] T. Fix *et al.*, J. Appl. Phys. **97**, 024907 (2005).

[59] M. Besse *et al.*, J. Crystal Growth **241**, 448 (2002).

[60] G. Haugstad, *Atomic Force Microscopy-Understanding Basic Modes and Advanced Applications* (John Wiley & Sons, 2012).

[61] J. G. Simmons, J. Appl. Phys. **34**, 2581 (1963).

[62] C. Julian Chen, *Introduction to Scanning Tunneling Microscopy* (Oxford University Press, 1993).

[63] P. Van der Heide, *X-ray photoelectron spectroscopy : an introduction to principles and practices* (Wiley, 2012).

[64] J. Als-Nielsen and D. McMorrow, *Elements of modern x-ray physics* (Wiley, 2010).

[65] S. R. Shinde *et al.*, J. Appl. Phys. **93**, 1605 (2003).

[66] M. Saloaro, S. Majumdar, H. Huhtinen, and P. Paturi, J. Phys. Cond. Mat. **24**, 366003 (2012).

[67] H. Jalili, N. F. Heinig, and K. T. Leung, J. Chem. Phys **132**, 204701 (2010).

[68] T.-Y. Cai and Z.-Y. Li, J. Phys. Cond. Mat. **16**, 3737 (2004).

[69] T. Manako *et al.*, Appl. Phys. Lett. **74**, 2215 (1999).

[70] A. Venimadhav *et al.*, Solid State Commun. **130**, 631 (2004).

[71] H. Boschker *et al.*, J. Phys. D: Appl. Phys. **44**, 205001 (2011).

[72] D. Kumar and D. Kaur, Journal of Alloys and Compounds **509**, 7886 (2011).

[73] E. Kukk *et al.*, Phys. Rev. A **63**, 062702 (2001).

[74] E. Kukk *et al.*, Phys. Rev. Lett. **95**, 133001 (2005).

[75] J. Devkota *et al.*, *Adv. Funct. Mater.*, 03 2016.

[76] H. Asano, *et al.*, , IEEE T. Magn., **41**:2811 – 2813, 2005.

[77] M. Bibes *et al.*, Appl. Phys. Lett., **83**, 2003.

[78] F. Wang, Chao Yang, and Xiaoguang Li. Phys. Rev. B, **75**, 2007.

[79] Z Xiong, Di Wu, and Jing Shi. Nature, **427**:821–4, 2004.

[80] W. H. Meiklejohn and C. P. Bean. Phys. Rev., **102**:1413–1414, 1956.

[81] T. Nguyen *et al.*, Phys. Rev. B, **87**, 2013.

[82] Da-Li Sun *et al.*, Phys. Rev. Lett., **104**:236602, 2010.

[83] S. Majumdar *et al.*, J. Alloy. Compd., **423**:169–171, 2006.

[84] H. Vinzelberg *et al.*, J. Appl. Phys., **103**:093720–093720, 2008.

[85] D. Sarma *et al.*, Phys. Rev. Lett., **85**:2549–52, 10 2000.

[86] M. Bibes *et al.*, Appl. Phys. Lett., **83**:2629, 2003.

[87] J. D. Teresa *et al.*, Science (New York), **286**:507 1999.

UNIVERSITY OF TURKU

Painosalama Oy, Turku, Finland 2020

ISBN 978-951-29-8138-0 (PRINT)
ISBN 978-951-29-8139-7 (PDF)
ISSN 0082-7002 (Print)
ISSN 2343-3175 (Online)